OXFORD

Journal of Petrology, 2023, **64**, 1–23
https://doi.org/10.1093/petrology/egad060
Advance access publication date 15 August 2023
Original Manuscript

Magnesian Andesites from Kibblewhite Volcano in the Kermadec Arc, New Zealand

Yasuhiro Hirai[1,2,3,*], Yoshihiko Tamura[2], Tomoki Sato[2], Takashi Miyazaki[2], Qing Chang[2], Bogdan S. Vaglarov[2], Jun-Ichi Kimura[2], Kaj Hoernle[4,5], Reinhard Werner[4], Folkmar Hauff[4] and Christian Timm[4,6]

[1]Division of Natural System, Kanazawa University, 920-1192 Ishikawa, Japan
[2]Research Institute for Marine Geodynamics, Japan Agency for Marine-Earth Science and Technology (JAMSTEC), 237-0061 Kanagawa, Japan
[3]Yoshida Junior High School, 369-1503 Saitama, Japan
[4]GEOMAR Helmholtz Centre for Ocean Research, 2418 Kiel, Germany
[5]Institute of Geosciences, Kiel University, 24118 Kiel, Germany
[6]GNS Science, PO Box, 30-268, 5010 Lower Hutt, New Zealand

*Corresponding author. Telephone: +81-494-77-0015. Fax: +81-494-77-0027. E-mail: deep.forest.alliance@gmail.com

Abstract

Primary andesitic magmas could be an important component of arc magma genesis and might have played a key role in the advent of continents. Recent studies hypothesized that primary andesitic magmas occur in the oceanic arc, where the crust is thin. The Kermadec arc has the thinnest crust among all the studied oceanic arcs (<15 km in thickness); however, there are no studies that corroborate the formation of primary andesitic magmas in the arc. The aim of this study is to develop a better understanding of primary andesites in oceanic arcs through the petrology of the Kermadec arc. Here, we present the petrology of volcanic rocks dredged from the Kibblewhite Volcano in the Kermadec arc during the R/V SONNE SO-255 expedition in 2017. Magma types range from andesite to rhyolite at the Kibblewhite Volcano, but basalts dominate at the neighboring cones. This study focuses on magnesian andesites from the northeastern flank of this volcano. The magnesian andesites are nearly aphyric and plagioclase free but contain microphenocrysts of olivine ($Fo_{84–86}$) and clinopyroxene (Mg# = 81–87). Using olivine addition models, the primary magmas were estimated to contain 55–56 wt % SiO_2 and 10–12 wt % MgO, similar to the high-Mg andesites observed in other convergent plate margins, indicating the generation of primary andesitic magma beneath the Kibblewhite Volcano. The trace element and isotopic characteristics of the magnesian andesites are typical of volcanic rocks from the Kermadec arc. This indicates that the subduction of a young plate or melting of a pyroxenitic source is not necessary to produce magnesian andesites. Instead, we propose that the magnesian andesites were produced by the direct melting of the uppermost mantle of the Kermadec arc. The thin crust of the Kermadec arc should yield low-pressure conditions in the uppermost mantle, allowing the sub-arc mantle to generate primary andesitic melts. This study supports the hypothesis that primary andesitic magmas generate in the arc where the crust is thin and provides a new insight into the magma genesis of the Kermadec arc.

Key words: high-Mg andesite; igneous petrology; primary magmas; Kermadec arc; subduction zone

INTRODUCTION

Mantle-derived primary magmas generated in volcanic arcs are generally basaltic, but primitive andesites have also been known to form in such settings. Primitive andesites from subduction zones are often referred to as high-magnesian andesites or high-Mg# andesites (HMA; Tatsumi & Ishizaka, 1982; Kelemen, 1995) and are believed to be closely related to the origin of the continental crust. Taylor (1967) proposed that the continental crust formed in subduction zones, based on the compositional similarity between continental crust and magnesian andesites found at convergent plate margins. Many studies (Taylor & McLennan, 1995; Rudnick & Gao, 2003) have also estimated that the average composition of the continental crust is similar to that of magnesian andesites (57–65 wt % SiO_2, 2.8–5.3 MgO, and FeO*/MgO = 1.4–2.2). Kelemen (1995) showed that the differentiation of primitive basaltic magmas cannot produce the average composition of continental crust and implied that the HMAs produced in subduction zones are the raw material of the continental crust. Thus, determining the origin of HMAs is important for understanding magma genesis in subduction zones and the development of the continental crust.

Two major models have been proposed to explain the origin of HMAs. The first model suggests that a notable contribution from Si-rich melts formed by the melting of the subducting slab is necessary to generate HMAs. This model requires specific conditions for the generation of HMAs, such as the subduction of a young plate (Defant & Drummond, 1990) and the melting of the eclogitic source (Straub *et al.*, 2008). Another model suggests that HMAs can be produced directly from the melting of the mantle at low pressures (Baker *et al.*, 1994; Grove *et al.*, 2003; Heyworth *et al.*, 2007). This model requires a thin crust such that low-pressure conditions exist in the uppermost mantle wedge. Tamura *et al.* (2016) noted that basaltic magmas are predominant where the crust is thick (30–35 km), whereas andesitic magmas tend to dominate where the crust is thin (15–20 km) in the Izu-Ogasawara and Aleutian oceanic arcs. Based on this relationship,

Received: January 8, 2023. **Revised:** August 6, 2023. **Accepted:** August 9, 2023

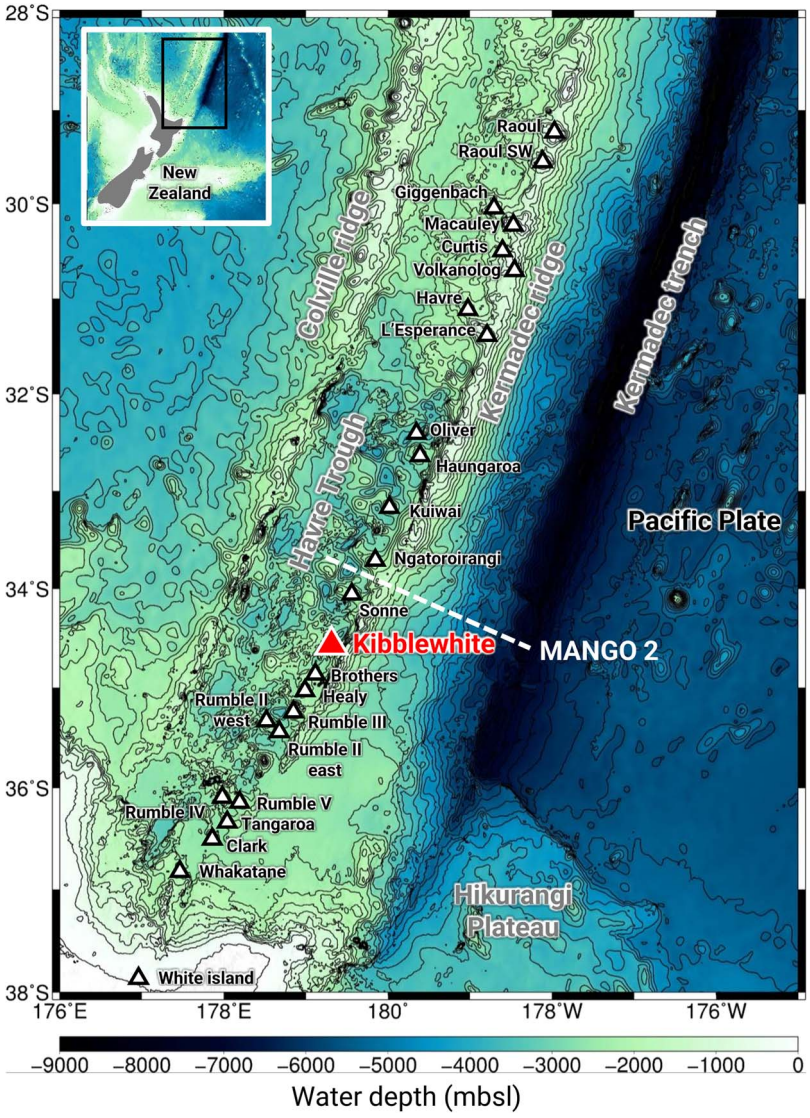

Fig. 1. Bathymetric map of the Kermadec arc system. Open triangles indicate the locations of Quaternary arc-front volcanoes of the Kermadec arc, with the red triangle highlighting the Kibblewhite Volcano (Wright *et al.*, 2006; de Ronde *et al.*, 2007). The dashed line indicates the MANGO 2 seismic refraction profile analyzed by Bassett *et al.* (2016).

they proposed a new hypothesis: only basaltic primary melts are produced beneath arc volcanoes where the crust is thick because the pressure of melting in the mantle is higher; however, if the crust is thin, mantle melting occurs at a lower pressure, resulting in the generation of primary andesitic magmas. Tamura *et al.* (2019) tested this hypothesis at the active Nishinoshima Volcano in the southern segment of the Izu-Ogasawara arc, where the crust is approximately 20 km thick, and described olivine-saturated andesites from this volcano. They concluded that the andesites were differentiated from primitive andesitic melts produced by low-pressure melting of the sub-arc mantle.

If the hypothesis of Tamura *et al.* (2016) is valid, then the HMA magmas should have been generated in the Kermadec arc. Crustal thicknesses beneath the arc-front volcanoes of the Kermadec arc range from ~9 to 12 km (Bassett *et al.*, 2016), which is similar to those of the Ogasawara arc in Japan (Kodaira *et al.*, 2007). In fact, olivine-saturated primitive andesites have been reported from the active White Island in the Taupo Volcanic Zone at the southernmost end of the Kermadec arc (Cole *et al.*, 2000). Heyworth *et al.* (2007) concluded that the White Island HMAs did not form by the partial melting of subducting slabs and could have been in equilibrium with mantle peridotite at 0.5–1.5 GPa, equivalent to the uppermost mantle of the Kermadec arc. This is the only reported HMA in the Kermadec arc. The bimodal magmatism of the basic (45–57 wt % SiO_2) and silicic (63–75 wt % SiO_2) magmas characterize the Kermadec arc, and andesitic magma is rare in the Kermadec arc (Smith *et al.*, 2003*a*; Wright *et al.*, 2006). However, as suggested by Kelemen *et al.* (2003*a*), it is likely that the relative amounts of magma that erupted on the surface do not necessarily represent their amounts at depth (Kuno, 1968). Thus, it is possible that there was a substantial volume of mantle-derived andesitic magma within the Kermadec arc.

A major question that arises from the related literature is whether there are other HMAs in the Kermadec arc. There are several volcanoes in this arc; however, most of them are submerged under the sea and have not been studied. During the expedition of SO-255 of the R/V SONNE, new volcanic rock samples were collected from the Kibblewhite Volcano, an arc-front volcano in the Kermadec arc. In this study, we present the petrology of volcanic rocks and discuss the origin of olivine-saturated magnesian andesites discovered on the northeastern flank of the Kibblewhite Volcano.

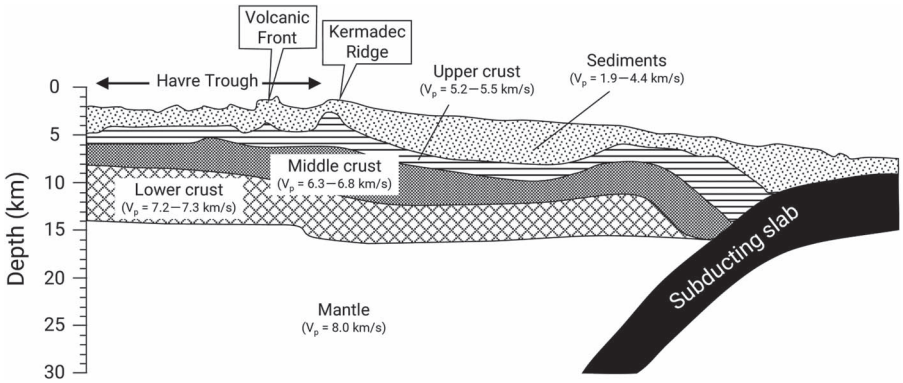

Fig. 2. Seismic across-arc crustal structure obtained from the MANGO 2 profile, passing between the Sonne and Ngatoroirangi volcanoes (modified from Bassett *et al.*, 2016). The crust–mantle boundary is at ~15 km below sea level beneath the arc front of the Kermadec arc.

GEOLOGICAL BACKGROUND

The Kermadec arc system (Fig. 1), produced by the subduction of the Pacific Plate beneath the Australian Plate, extends approximately 2500 km from New Zealand to Tonga. The subduction of the Pacific plate has also caused the opening of the Havre trough, which has split the proto-Kermadec arc (the Vitiaz arc) edifice into the Colville and Kermadec ridges at 4.41 ± 0.35 Ma (Timm *et al.*, 2019; Hoernle *et al.*, 2021). Hydrothermal activity has been observed at ~75% of the major 33 arc-front volcanoes, indicating that the Kermadec arc is one of the most active volcanic arcs worldwide (de Ronde *et al.*, 2007). Recently, an extensive dataset of Havre trough lavas was reported, including HMA samples from the Kibblewhite Volcano (Gill *et al.*, 2021; Hauff *et al.*, 2021).

Bassett *et al.* (2016) presented the across-arc seismic refraction profiles (MANGO profiles) of the Kermadec arc system. Fig. 2 shows the P-wave seismic structure of the MANGO 2 profile passing between the Sonne and Ngatoroirangi volcanoes. According to this study, the total crustal thickness is ~12 km, and the crust–mantle boundary is located ~15 km below sea level. Other oceanic arcs, such as the Tonga arc (~17 km; Contreras-Reyes *et al.*, 2011), South Sandwich arc (~20 km; Larter *et al.*, 2003), Izu and Ogasawara arcs (~30 and ~20 km, respectively; Kodaira *et al.*, 2007), and Mariana arc (~20 km; Takahashi *et al.*, 2007; Calvert *et al.*, 2008), have greater crustal thicknesses. This indicates that the Kermadec arc could have the thinnest crust among oceanic arcs and thus may be unique among oceanic arcs.

Kibblewhite Volcano is located between the Sonne and Brothers volcanoes on the volcanic front (Fig. 1) and is surrounded by several volcanic cones (Fig. 3; Hoernle *et al.*, 2017). Detailed seafloor mapping and a volcanological study of the Kibblewhite Volcano were first performed by Wright *et al.* (2006). The Kibblewhite Volcano has ~1000 m of relief, a 13-km-diameter base at ~2500 m of water depth, and a volume of 47.8 km^3. Hydrothermally altered lava breccias were observed on the upper southern flank of the Kibblewhite Volcano using a deep-tow camera, suggesting active submarine volcanism (Wright *et al.*, 2006). The cones neighboring the volcano were KI1, KI2, KI3, and KI4 (Fig. 3). These cones have ~700–950 m of relief, ~3.5- to 6.0-km-diameter bases at ~2000–2500 m of water depths, and volumes of 2.3–8.9 km^3 (Wright *et al.*, 2006).

The 35 volcanic rock samples analyzed in this study were collected during the SO-255 R/V SONNE expedition carried out in 2017, through the process of dredging (Hoernle *et al.*, 2017). The dredging locations are shown in Fig. 3. Four dredge surveys were conducted around the central cone of Kibblewhite: two on a NE–SW trending fissure ridge extending from the NE flank (DR24 and DR25), one on the upper section of the SW flank (DR26), and another on a NE–SW trending tectonic feature extending from the southern flank (DR27). Four dredges were conducted on neighboring cones KI1 (DR22), KI3 (DR29), KI4 (DR28), and 'unnamed' tiny cones (DR23). Data from additional samples from these locations have been reported by Gill *et al.* (2021) and Hauff *et al.* (2021).

ANALYTICAL METHODS

Mineral and glass chemistry

The chemical compositions of the minerals were determined using an electron probe microanalyzer (EPMA; JEOL JXA-8500F Superprobe) equipped with five wavelength-dispersive spectrometers at the Japan Agency for Marine-Earth Science and Technology (JAMSTEC). The olivine was analyzed at an accelerating voltage of 20 kV, a 25-nA beam current, and 5-μm beam diameter. The counting times were 20 s on the peak and 10 s on the background for Si, Ti, Al, Fe, and Mg; and 100 s on the peak and 50 s on the background for Mn, Ca, and Ni. The two standard deviations of the mean (2σ) for MnO, CaO, and NiO in the in-house olivine standards were ±0.007, ±0.011, and ±0.013 wt % ($n = 9$), respectively, during the measurement period. Other minerals were analyzed using a 15-kV accelerating voltage, 12-nA beam current, and 1- to 5-μm beam diameter, and depending on the size of the material, with 20 s on the peak and 10 s on the background. The measured chemical compositions of the minerals in the volcanic rocks from the Kibblewhite Volcano are presented in Table S1.

Quenched glass from the chilled margin of the andesite lavas collected from DR25 was also analyzed by an EPMA. These glasses were analyzed using a 15-kV accelerating voltage, 10-nA beam current, and 10-μm beam diameter. Counting times were 10 s on the peak and 5 s on the background for Na and K; 20 s on the peak and 10 s on the background for Si, Ti, Al, Fe, Mg, Ca, and P; and 100 s on the peak and 50 s on the background for Cl and S. Na and K were measured first to avoid Na loss during the measurement (Morgan & London, 1996).

Whole-rock chemistry

Rock samples were crushed into pebbles (5–10 mm) using an iron hammer. These crushed chips were soaked in water at ~40°C for 2 weeks. The chips were then boiled in distilled water in a microwave oven. Successful desalinization was confirmed by the addition of a silver nitrate solution to the water. If silver

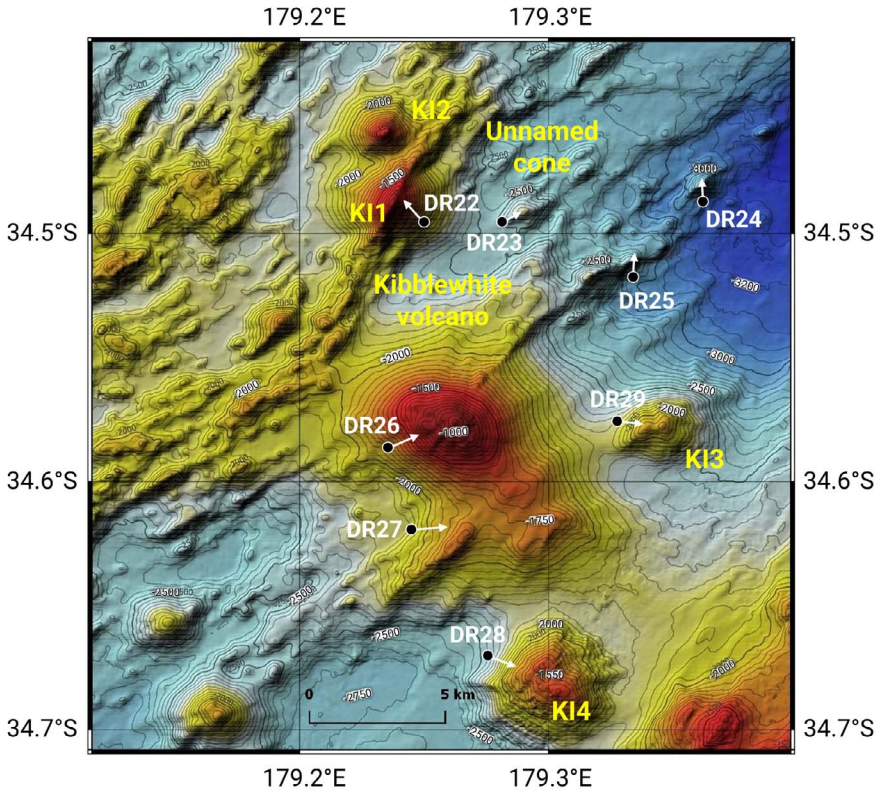

Fig. 3. Bathymetric map of the Kibblewhite Volcano and the locations of dredge samplings. Kibblewhite is a stratovolcano, surrounded by several volcanic cones. Black dots with white arrows indicate the off-bottom locations and directions of dredge sampling, respectively. The most prominent cones are KI1 to KI4 (Wright *et al.*, 2006). 'Unnamed' tiny cone was also dredged (DR23) in this study.

chloride precipitated in the water, the boiling was repeated. After desalinization, all samples were sonicated in acetone for cleaning. These samples were coarsely pounded in an iron mortar and as many altered pieces as possible were manually removed. All the samples were further pulverized in a vibration mill (Multi-Beads Shocker; Yasui Kikai Co., Osaka, Japan) using a polycarbonate capsule with a 50-cm^3 inner volume and a high-purity alumina rod to prepare the bulk rock powder.

The major and selected trace elements (V, Cr, Ni, Cu, Zn, Rb, Sr, Ba, Y, Zr, and Nb) were determined by X-ray fluorescence (XRF), using ZSX Primus II (Rigaku Co., Tokyo, Japan) and RIX 3000 (Rigaku Co.) at JAMSTEC. The major elements were analyzed on glass beads made from a mixture of 0.4-g sample powder and 4-g anhydrous $Li_2B_4O_7$, and the trace elements were analyzed on pressed powder discs (Tani *et al.*, 2005). All data discussed below are shown as values normalized to 100% on a volatile-free basis, with the total Fe calculated as FeO*.

Trace elements, including rare earth elements (REEs), Sc, Ni, Rb, Sr, Y, Zr, Nb, Cs, Ba, Hf, Ta, Pb, Th, and U, were analyzed by inductively coupled plasma mass spectrometry (ICP-MS), using the Agilent 7500a (Agilent Technologies Inc., Santa Clara, CA, USA) and iCAPQ (Thermo Fisher Scientific Inc., Waltham, MA, USA) models at JAMSTEC. Samples for analysis were prepared as per a previously reported method (Chang *et al.*, 2003). Approximately 100 mg of the sample powder was dissolved in an HF–$HClO_4$ acid mixture (3:1). After drying, the residue was dissolved in $HClO_4$. After evaporation, the residue was dissolved in 6 N HNO_3 and dried. Finally, the residues were dissolved in 2% HNO_3 at a 10 000–20 000 dilution factor for analysis. In and Bi were added to the solution as internal standards. Reproducibility in the analysis of the reference material (JB-2; Geological Survey of Japan) was generally better than ±2% two standard deviations (2 SD), except for Nb (±4.1%, 2 SD) in the Agilent 7500a and Ta (±3.0%, 2 SD) in the iCAPQ. The relative difference between Agilent 7500a and iCAPQ in the analysis of the JB-2 standard was generally <5%, except for Nb (6.7%) and Ta (25.5%).

For the analysis of the Sr, Nd, Pb, and Hf isotopic ratios, the sample powders were leached using a mixture of 6 N HCl and 1 N HF, rinsed using Milli-Q water (Merck KGaA, Darmstadt, Germany) and then dried. Approximately 100 mg of the residues were used for the chemical digestion and separation; the detailed sample digestion and chemical separation procedures are described in Miyazaki *et al.* (2018). Column separation procedures were conducted using the fully automated open-column chemical separation system COLUMNSPIDER (HOYUTEC Co., Ltd., Kawagoe, Japan) developed by JAMSTEC (Miyazaki *et al.*, 2012). Total procedural blanks for Sr, Nd, Pb, and Hf were <300, <10, <5, and <15 pg, respectively. The isotopic ratios of Sr and Nd were determined at JAMSTEC, using thermal ionization mass spectrometry on a Triton TI mass spectrometer (Thermo Fisher Scientific Inc.). The isotope ratios were normalized to $^{86}Sr/^{88}Sr = 0.1194$ and $^{146}Nd/^{144}Nd = 0.7219$. The measured values for the National Institute of Standards and Technology (NIST) Standard Reference Material (SRM)-987 and JNdi-1 were $^{87}Sr/^{86}Sr = 0.710248 \pm 0.000020$ (2 SD, $n = 12$) and $^{143}Nd/^{144}Nd = 0.512096 \pm 0.000018$ (2 SD, $n = 8$) during the measurement period. The $^{87}Sr/^{86}Sr$ and $^{143}Nd/^{144}Nd$ data in this study were reported without normalization. The isotopic ratios of Pb and Hf were determined using a multi-collector-ICP-MS (Thermo Fisher Scientific Neptune, Thermo Fisher Scientific) at JAMSTEC. The mass fractionation factors for Pb were corrected using Tl as an external standard. Mass-dependent inter-element

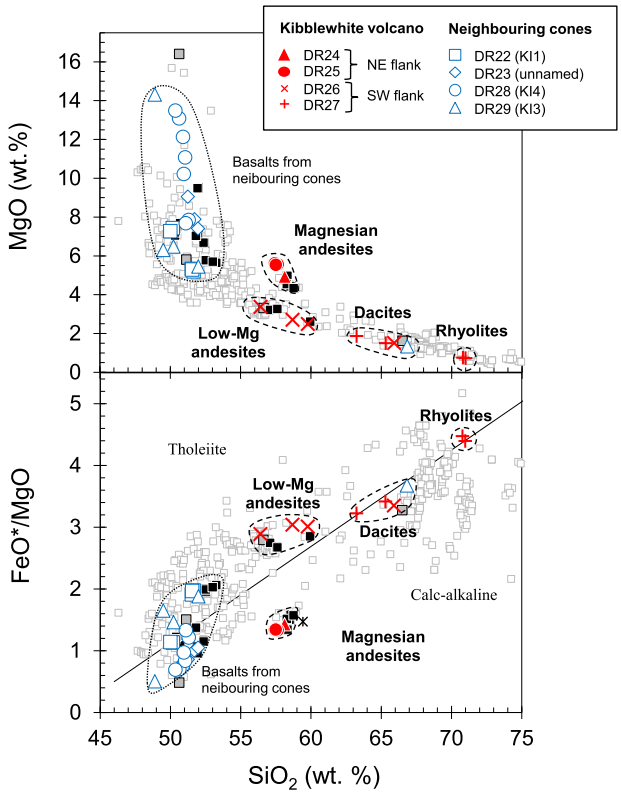

Fig. 4. Variations of MgO and FeO*MgO versus SiO_2 for volcanic rocks from the Kibblewhite Volcano and neighboring cones. The discrimination boundary line in FeO*/MgO-SiO_2 diagram is from Miyashiro (1974). Open gray squares are volcanic rocks from the Kermadec arc front (Gamble *et al.*, 1993, 1996, 1997; Ewart *et al.*, 1994; Turner *et al.*, 1997; Haase *et al.*, 2002; Wright *et al.*, 2006; Barker *et al.*, 2013; Timm *et al.*, 2014, 2016). Filled gray and black squares represent the published data for Kibblewhite Volcano from Wright *et al.* (2006) and Hauff *et al.* (2021).

fractionations were corrected by applying a standard bracketing method using NIST SRM-981 as the standard (Kimura *et al.*, 2006). The repeated measurements of $^{206}Pb/^{204}Pb$, $^{207}Pb/^{204}Pb$, and $^{208}Pb/^{204}Pb$ for SRM-981 were 16.9294 ± 0.0045, 15.4818 ± 0.0063, and 36.6678 ± 0.0184 (2 SD, $n = 24$), respectively, during the measurement period. All Pb isotope data were obtained after normalization using the SRM-981 values of $^{206}Pb/^{204}Pb = 16.9416$, $^{207}Pb/^{204}Pb = 15.5000$, and $^{208}Pb/^{204}Pb = 36.7262$ (Baker *et al.*, 2004). The mass fractionation factors for Hf were corrected using $^{179}Hf/^{177}Hf$, and the isotope ratios were normalized to $^{179}Hf/^{177}Hf = 0.7325$ (Patchett & Tatsumoto, 1981). The ^{173}Yb and ^{175}Lu peaks were monitored during measurement to correct for interference from ^{176}Yb and ^{176}Lu on the ^{176}Hf peak and were always undetectable. The repeated measurements of $^{176}Hf/^{177}Hf$ in JMC475 were 0.282146 ± 0.000015 (2 SD, $n = 20$) during the measurement period. The reported $^{176}Hf/^{177}Hf$ ratio was adjusted to a JMC475 value of $^{176}Hf/^{177}Hf = 0.28216$ (Vervoort & Blichert-Toft, 1999) using a standard bracketing method.

The whole-rock major, trace, and Sr–Nd–Hf–Pb isotopic compositions of the samples are listed in Table 1. The results of the standard reference materials for the Sr–Nd–Hf–Pb isotope analyses obtained during the analytical session are presented in Table S2. The results of the trace elements and Sr–Nd–Hf–Pb isotope analyses for the JB-2 basalt standard are listed in Table S3.

RESULTS

Magmatic variations of the Kibblewhite Volcano

Based on petrography, mineral chemistry, and whole-rock geochemistry, we divided the volcanic rocks from the Kibblewhite Volcano and neighboring cones into five groups. Fig. 4 shows the variations in MgO and FeO*/MgO with SiO_2 for the magmatic groups. The magnesian andesites (57.6–58.1 wt % SiO_2; 4.9–5.6 wt % MgO) are from the fissure ridge on the NE flank of Kibblewhite Volcano and show higher MgO contents at a given SiO_2 content than low-Mg andesites (56.4–59.8 wt % SiO_2; 2.5–3.4 wt % MgO) that were collected on the SW flank. The magnesian andesites are also characterized by lower FeO*/MgO ratios than the low-Mg andesites (Fig. 4). Pumiceous rocks mainly recovered from the southern and southwestern flank of the Kibblewhite Volcano are dacites (63.2–66.8 SiO_2; 1.3–1.9 wt % MgO) and rhyolites (70.8–71.0 SiO_2; 0.7–0.8 wt % MgO), but it is not clear if these rocks originated from Kibblewhite or another arc front (or possibly rear/backarc) volcano (Gill *et al.*, 2021). The neighboring cones consist mainly of basalts (48.9–52.0 wt % SiO_2; 5.5–14.3 wt % MgO; Fig. 4). Samples previously reported by Wright *et al.* (2006), collected from the summit of the Kibblewhite Volcano, are classified as low-Mg andesite and dacite (filled gray squares in Fig. 4). Recently published data for the Kibblewhite Volcano (Gill *et al.*, 2021; Hauff *et al.*, 2021) are consistent with the data from this study, including basalts, magnesian andesites, and low-Mg andesites (black squares in Fig. 4).

Petrography and mineral chemistry

Magnesian andesites

Magnesian andesites are highly vesiculated lavas (Fig. 5a) accompanied by quenched glass rinds. Neither Mn nor sediment coating is observed on the glassy rock surfaces. These lavas contain olivine and clinopyroxene microphenocrysts (<0.4 mm) in groundmasses composed of dendritic clinopyroxene and glass (Fig. 5b). Plagioclase is absent even in the groundmasses. Olivine microphenocrysts often show skeletal shapes, suggesting quenched crystallization, and have limited forsterite content (Fo: 100 Mg/[Mg + Fe]) in equilibrium with whole-rock compositions ($Fo_{83–86}$; Fig. S1a). The clinopyroxene microphenocrysts show a similar Mg# (100 Mg/[Mg + Fe]) to that of the olivine microphenocrysts (82–87; Fig. S1). Relatively large olivine crystals are sparse (>0.5 mm; 1–2 vol %; Fig. 5a) and have forsteritic cores ($Fo_{90–93}$) surrounded by thin rims that have similar compositions to the olivine microphenocrysts ($Fo_{84–85}$), indicating their xenocrystic origin (Fig. 5c). Chromian spinels with high Cr# (Cr/[Cr + Al]; 69–81) are also observed in the olivine xenocrysts.

Another magnesian andesite (DR24-1) is aphyric, poorly vesiculated, and composed of clinopyroxene and plagioclase (Fig. 5d). Groundmass clinopyroxenes have Mg# values similar to those of the magnesian andesites from DR25 (Mg# = 83–85; Fig. S1). Dendritic groundmass plagioclases show a narrow range of anorthite contents ($An_{66–71}$; Fig. S1a). The relatively large clinopyroxene crystals are sparse. These have Fe-rich resorbed internal cores (Mg# = 70–80) mantled by magnesian rims (Mg# = 80–86), indicating a xenocrystic origin (Fig. 5e). A dissolved orthopyroxene xenocryst (Mg# = 68) with a thin magnesian rim (Mg# = 81) was also observed (Fig. 5f). These xenocrysts indicate that this magma interacted with a more differentiated magma and felsic crustal material before the eruption and therefore did not represent magnesian andesite.

Table 1: Whole-rock major trace element and Sr–Nd–Hf–Pb isotope compositions of volcanic rocks from the Kibblewhite Volcano and neighboring cones

Sample ID:	**DR22-1**	**DR22-2**	**DR22-3**	**DR22-4**	**DR22-5**	**DR23-1**	**DR23-2**	**DR23-4**	**DR24-1**
Latitude(°S)	**34.50**	**34.50**	**34.50**	**34.50**	**34.50**	**34.50**	**34.50**	**34.50**	**34.49**
Longitude(°E)	**179.24**	**179.24**	**179.24**	**179.24**	**179.24**	**179.29**	**179.29**	**179.29**	**179.36**
Depth (m)	**1780**	**1780**	**1780**	**1780**	**1780**	**2476**	**2476**	**2476**	**3081**
Major elements (XRF) wt %									
SiO_2	49.50	49.35	50.71	50.77	50.35	50.54	50.79	51.26	57.31
TiO_2	0.70	0.68	1.05	1.08	1.07	0.84	0.91	0.93	0.71
Al_2O_3	16.91	17.36	17.17	17.00	16.78	16.26	16.53	16.77	15.78
Fe_2O_3	9.22	9.08	11.12	11.21	11.29	8.51	8.62	8.52	7.73
MnO	0.16	0.15	0.18	0.18	0.18	0.14	0.15	0.14	0.15
MgO	7.33	7.17	5.24	5.11	5.17	8.93	7.75	7.31	4.87
CaO	13.55	13.59	10.80	10.81	10.73	11.59	11.57	11.66	8.51
Na_2O	1.79	1.79	2.63	2.66	2.63	2.06	2.14	2.21	2.80
K_2O	0.33	0.32	0.49	0.44	0.44	0.45	0.47	0.52	1.38
P_2O_5	0.11	0.11	0.15	0.15	0.15	0.15	0.16	0.16	0.13
Total	99.59	99.59	99.52	99.40	98.80	99.47	99.08	99.48	99.36
Trace elements (XRF) ppm									
V	267.2	264.0	317.7	319.9	321.1	254.5	274.2	279.3	201.8
Cr	155.4	123.3	12.8	9.5	11.1	335.0	275.5	199.5	101.5
Ni	61.0	55.4	19.1	18.1	19.7	133.3	98.3	73.1	37.7
Cu	111.3	104.2	131.0	132.3	131.5	67.2	77.5	70.1	64.8
Zn	62.4	62.4	82.2	82.1	81.8	62.3	65.7	63.1	69.2
Rb	7.2	7.3	9.1	9.2	8.8	7.6	8.1	8.5	26.2
Sr	201.7	204.5	220.0	219.8	219.7	241.9	251.7	259.1	187.9
Ba	134.0	156.2	135.7	153.1	144.2	115.2	131.7	143.2	318.5
Y	14.2	13.4	19.9	20.7	19.5	15.6	15.7	16.7	23.8
Zr	37.4	37.0	63.9	65.8	64.7	56.2	60.5	62.2	95.5
Nb	1.3	1.3	1.8	1.9	1.8	5.6	6.3	6.0	2.2
Trace elements (ICP-MS) ppm									
(machine)	iCAPQ	iCAPQ	iCAPQ	iCAPQ		7900a	iCAPQ	iCAPQ	iCAPQ
Sc	36.1	35.2	28.6	28.8	—	33.1	30.1	30.2	21.8
Ni	56.8	54.3	20.1	18.2	—	127.3	98.2	81.0	34.3
Rb	5.9	5.9	7.4	7.4	—	5.7	6.3	6.7	22.5
Sr	207.3	212.4	222.5	225.2	—	237.2	252.7	256.8	183.3
Y	13.5	13.2	18.9	19.4	—	14.4	15.1	15.3	21.3
Zr	36.4	35.3	62.5	63.6	—	55.1	58.4	58.7	89.8
Nb rec	0.95	0.93	1.50	1.61	—	4.99	5.41	5.38	2.01
Cs	0.25	0.24	0.25	0.26	—	0.20	0.20	0.20	0.85
Ba	126.4	125.7	142.5	147.6	—	121.4	125.4	129.4	298.5
La	3.31	3.23	4.56	4.66	—	5.26	5.79	5.81	7.09
Ce	8.08	7.93	11.63	11.92	—	11.95	13.30	13.40	16.93
Pr	1.22	1.20	1.75	1.80	—	1.67	1.83	1.86	2.41
Nd	6.14	6.07	8.84	9.06	—	7.63	8.50	8.66	11.24
Sm	1.87	1.84	2.62	2.72	—	2.11	2.28	2.35	3.05
Eu	0.68	0.64	0.95	0.94	—	0.69	0.81	0.81	0.90
Gd rec	2.29	2.25	3.29	3.38	—	2.47	2.70	2.76	3.55
Tb	0.40	0.39	0.57	0.58	—	0.43	0.45	0.47	0.61
Dy	2.59	2.56	3.67	3.77	—	2.69	2.92	3.02	3.94
Ho	0.54	0.54	0.78	0.80	—	0.57	0.61	0.63	0.85
Er	1.63	1.59	2.29	2.37	—	1.67	1.80	1.87	2.55
Tm	0.22	0.22	0.32	0.34	—	0.24	0.25	0.26	0.37
Yb	1.52	1.48	2.16	2.23	—	1.58	1.72	1.75	2.56
Lu	0.22	0.22	0.32	0.33	—	0.24	0.25	0.26	0.39
Hf	1.08	1.07	1.74	1.80	—	1.43	1.53	1.57	2.49
Ta	0.049	0.052	0.089	0.102	—	0.328	0.335	0.351	0.120
Pb	1.35	1.34	1.67	1.72	—	1.23	1.40	1.69	2.69
Th	0.530	0.518	0.675	0.705	—	0.642	0.685	0.696	1.358
U	0.170	0.165	0.216	0.228	—	0.227	0.266	0.242	0.475
Isotopes									
$^{87}Sr/^{86}Sr$	0.703625	—	0.703338	—	—	0.703415	—	—	0.703558
(2SE)	*0.000009*	—	*0.000009*	—	—	*0.000009*	—	—	*0.000007*
$^{143}Nd/^{144}Nd$	0.512980	—	0.513008	—	—	0.512999	—	—	0.512965
(2SE)	*0.000009*	—	*0.000009*	—	—	*0.000009*	—	—	*0.000009*
$^{176}Hf/^{177}Hf$	0.283160	—	0.283164	—	—	0.283125	—	—	0.283143

(Continued)

Table 1: Continued

(2SE)	*0.000006*	—	*0.000006*	—	—	*0.000005*	—	—	*0.000005*
$^{206}Pb/^{204}Pb$	18.819	—	18.816	—	—	18.845	—	—	18.840
(2SE)	*0.006*	—	*0.001*	—	—	*0.001*	—	—	*0.001*
$^{207}Pb/^{204}Pb$	15.627	—	15.619	—	—	15.609	—	—	15.628
(2SE)	*0.005*	—	*0.001*	—	—	*0.001*	—	—	*0.001*
$^{208}Pb/^{204}Pb$	38.668	—	38.647	—	—	38.647	—	—	38.688
(2SE)	*0.013*	—	*0.002*	—	—	*0.002*	—	—	*0.002*
Sample ID:	**DR25-1**	**DR25-2**	**DR25-3**	**DR26-1**	**DR26-2**	**DR26-3**	**DR26-16**	**DR27-1**	**DR27-5**
Latitude(°S)	**34.52**	**34.52**	**34.52**	**34.58**	**34.58**	**34.58**	**34.58**	**34.62**	**34.62**
Longitude(°E)	**179.33**	**179.33**	**179.33**	**179.24**	**179.24**	**179.24**	**179.24**	**179.25**	**179.25**
Depth (m)	**2896**	**2896**	**2896**	**1511**	**1511**	**1511**	**1511**	**1934**	**1934**
Major elements (XRF) wt %									
SiO_2	56.78	56.52	56.72	58.99	55.20	57.99	65.00	70.01	64.39
TiO_2	0.73	0.73	0.72	0.96	1.10	1.02	0.71	0.51	0.72
Al_2O_3	15.22	15.14	15.17	16.87	16.48	16.78	15.64	14.37	15.96
Fe_2O_3	8.16	8.23	8.09	8.22	10.62	9.04	5.54	3.53	5.63
MnO	0.15	0.15	0.15	0.20	0.21	0.20	0.14	0.12	0.14
MgO	5.48	5.47	5.47	2.46	3.31	2.68	1.49	0.72	1.48
CaO	8.82	8.81	8.80	6.53	7.75	6.87	4.40	2.96	4.50
Na_2O	2.81	2.80	2.84	3.53	3.27	3.43	4.36	4.56	4.40
K_2O	1.11	1.13	1.12	1.56	0.79	1.49	1.72	2.10	1.75
P_2O_5	0.15	0.15	0.15	0.21	0.19	0.23	0.18	0.11	0.19
Total	99.40	99.12	99.22	99.52	98.92	99.72	99.19	98.99	99.17
Trace elements (XRF) ppm									
V	229.9	221.0	216.0	102.3	186.4	120.5	67.7	21.8	71.3
Cr	163.6	180.5	158.4	5.2	6.6	6.8	8.4	5.8	4.9
Ni	49.8	46.8	49.4	0.0	0.0	0.0	0.0	6.8	4.8
Cu	85.4	78.6	80.4	19.8	14.6	13.0	17.3	28.4	13.4
Zn	72.0	72.6	72.1	83.3	88.1	81.6	71.1	68.9	67.1
Rb	24.3	24.9	25.0	31.5	18.7	25.0	44.3	48.3	42.1
Sr	196.8	197.4	197.5	252.7	249.4	253.5	199.4	144.7	210.6
Ba	335.1	345.5	350.0	368.6	291.4	319.8	548.1	675.5	511.8
Y	22.6	22.7	22.4	28.0	24.3	26.5	33.3	40.1	33.4
Zr	87.1	87.5	87.2	87.9	68.8	81.3	151.5	177.1	145.2
Nb	2.1	2.0	2.2	2.1	1.7	2.1	3.5	3.8	3.2
Trace elements (ICP-MS) ppm									
	7900a	iCAPQ	iCAPQ	iCAPQ	iCAPQ		iCAPQ	iCAPQ	iCAPQ
Sc	27.2	24.8	24.5	13.8	19.6	—	6.6	1.3	7.4
Ni	46.6	44.9	44.1	2.6	0.5	—	1.5	1.9	1.2
Rb	21.9	21.9	21.7	26.4	15.5	—	37.7	40.3	35.2
Sr	188.2	197.3	196.8	242.9	240.5	—	187.7	134.2	197.5
Y	21.2	21.0	20.7	25.2	22.0	—	30.2	34.4	29.8
Zr	85.0	83.8	82.7	80.7	64.4	—	133.4	153.4	126.4
Nb rec	1.94	1.90	1.87	1.76	1.40	—	3.02	3.45	2.84
Cs	0.84	0.85	0.84	0.87	0.62	—	1.40	1.73	1.28
Ba	337.0	326.0	327.2	333.1	246.0	—	496.0	611.3	474.4
La	7.22	7.36	7.27	6.98	5.47	—	11.18	11.77	10.63
Ce	16.84	17.44	17.16	17.28	13.73	—	26.43	28.13	25.43
Pr	2.40	2.45	2.44	2.60	2.04	—	3.70	4.01	3.61
Nd	11.13	11.50	11.40	12.74	10.33	—	16.92	18.55	16.74
Sm	3.07	3.08	3.11	3.62	3.02	—	4.44	4.95	4.50
Eu	0.88	0.93	0.86	1.17	1.07	—	1.25	1.10	1.20
Gd rec	3.47	3.49	3.55	4.37	3.80	—	5.00	5.60	5.09
Tb	0.60	0.61	0.60	0.74	0.64	—	0.86	0.96	0.87
Dy	3.82	3.89	3.91	4.84	4.20	—	5.45	6.27	5.56
Ho	0.82	0.82	0.84	1.03	0.89	—	1.17	1.37	1.20
Er	2.45	2.52	2.54	3.09	2.70	—	3.61	4.22	3.67
Tm	0.36	0.36	0.37	0.45	0.38	—	0.52	0.63	0.53
Yb	2.43	2.50	2.49	3.00	2.59	—	3.62	4.34	3.66
Lu	0.39	0.38	0.38	0.46	0.39	—	0.55	0.67	0.56
Hf	2.34	2.33	2.34	2.34	1.86	—	3.66	4.34	3.60
Ta	0.124	0.111	0.114	0.108	0.076	—	0.182	0.214	0.180
Pb	2.89	2.87	2.86	2.85	2.20	—	4.12	5.20	3.96
Th	1.431	1.412	1.413	1.084	0.801	—	2.195	2.240	2.061
U	0.479	0.468	0.462	0.528	0.338	—	0.741	0.841	0.699

(Continued)

Table 1: Continued

Isotopes									
$^{87}Sr/^{86}Sr$	0.703676	—	—	0.703645	0.703670	—	—	0.703749	—
(2SE)	0.000008	—	—	0.000006	0.000007	—	—	0.000008	—
$^{143}Nd/^{144}Nd$	0.512960	—	—	0.512977	0.512979	—	—	0.512929	—
(2SE)	0.000009	—	—	0.000008	0.000009	—	—	0.000009	—
$^{176}Hf/^{177}Hf$	0.283139	—	—	0.283165	0.283164	—	—	0.283151	—
(2SE)	0.000005	—	—	0.000005	0.000006	—	—	0.000005	—
$^{206}Pb/^{204}Pb$	18.845	—	—	18.838	18.843	—	—	18.848	—
(2SE)	0.001	—	—	0.001	0.001	—	—	0.001	—
$^{207}Pb/^{204}Pb$	15.630	—	—	15.622	15.626	—	—	15.624	—
(2SE)	0.001	—	—	0.001	0.001	—	—	0.001	—
$^{208}Pb/^{204}Pb$	38.700	—	—	38.671	38.685	—	—	38.675	—
(2SE)	0.002	—	—	0.003	0.003	—	—	0.003	—
Sample ID:	**DR27-7**	**DR27-9**	**DR28-1**	**DR28-10**	**DR28-12**	**DR28-17**	**DR28-22**	**DR28-25**	**DR28-26**
Latitude(°S)	**34.62**	**34.62**	**34.67**	**34.67**	**34.67**	**34.67**	**34.67**	**34.67**	**34.67**
Longitude(°E)	**179.25**	**179.25**	**179.28**	**179.28**	**179.28**	**179.28**	**179.28**	**179.28**	**179.28**
Depth (m)	**1934**	**1934**	**2221**	**2221**	**2221**	**2221**	**2221**	**2221**	**2221**
Major elements (XRF) wt %									
SiO_2	69.92	62.29	50.15	49.97	50.28	50.18	50.49	49.68	50.24
TiO_2	0.52	0.81	0.55	0.53	0.58	0.62	0.62	0.55	0.66
Al_2O_3	14.40	16.29	12.03	11.53	12.83	13.51	14.84	11.84	14.96
Fe_2O_3	3.72	6.60	10.13	10.03	10.11	10.85	10.41	10.22	11.17
MnO	0.11	0.15	0.17	0.17	0.17	0.19	0.18	0.17	0.19
MgO	0.75	1.84	11.95	12.91	10.91	10.06	7.73	13.30	7.55
CaO	2.91	5.21	12.72	12.83	12.69	12.01	12.82	12.12	12.18
Na_2O	4.49	4.29	1.45	1.38	1.55	1.69	1.63	1.43	1.69
K_2O	2.21	1.46	0.30	0.28	0.31	0.34	0.59	0.29	0.63
P_2O_5	0.12	0.22	0.08	0.08	0.08	0.09	0.14	0.08	0.15
Total	99.15	99.16	99.55	99.69	99.51	99.55	99.46	99.66	99.42
Trace elements (XRF) ppm									
V	32.5	86.7	276.0	261.7	284.3	295.8	302.7	276.4	315.9
Cr	4.3	8.1	595.9	650.9	504.6	328.0	203.6	678.8	151.0
Ni	5.4	0.0	130.0	147.0	118.0	102.0	48.4	172.9	54.3
Cu	20.4	18.8	92.2	74.2	89.6	92.8	109.8	95.0	119.7
Zn	68.2	64.7	70.4	67.2	72.2	79.0	73.1	69.8	79.7
Rb	56.5	33.4	5.7	5.4	5.8	6.5	14.3	6.1	14.5
Sr	162.5	231.0	141.0	132.3	147.5	158.2	236.5	138.6	241.1
Ba	676.4	450.9	163.8	150.0	171.2	162.1	388.9	145.1	399.3
Y	39.8	32.2	12.5	11.8	12.8	13.9	13.8	12.0	14.8
Zr	201.4	123.1	29.9	27.8	30.9	33.4	34.3	29.0	36.2
Nb	4.0	2.7	0.6	0.5	0.5	0.5	0.7	0.5	0.7
Trace elements (ICP-MS) ppm									
	iCAPQ	iCAPQ			iCAPQ	iCAPQ	iCAPQ	7900a	iCAPQ
Sc	2.2	11.0	—	—	41.2	39.4	42.3	43.0	43.2
Ni	0.8	1.1	—	—	108.4	99.3	47.0	176.4	52.3
Rb	49.0	27.7	—	—	4.3	4.7	12.2	4.4	13.7
Sr	153.0	219.1	—	—	150.4	161.1	214.8	136.8	251.4
Y	36.2	29.0	—	—	11.9	13.0	13.5	11.6	14.9
Zr	176.5	110.4	—	—	29.0	32.0	33.1	28.3	37.2
Nb rec	3.88	2.42	—	—	0.40	0.45	0.50	0.41	0.59
Cs	1.74	0.99	—	—	0.21	0.23	0.44	0.23	0.51
Ba	631.8	395.0	—	—	148.3	160.2	353.9	141.0	408.0
La	14.51	8.99	—	—	1.77	1.99	5.03	1.66	5.69
Ce	33.69	21.93	—	—	4.81	5.26	10.83	4.42	12.23
Pr	4.65	3.20	—	—	0.79	0.86	1.60	0.73	1.83
Nd	20.68	15.35	—	—	4.24	4.58	7.71	3.86	8.82
Sm	5.27	4.23	—	—	1.42	1.53	2.18	1.30	2.47
Eu	1.30	1.24	—	—	0.49	0.55	0.71	0.46	0.71
Gd rec	5.86	5.00	—	—	1.91	2.04	2.53	1.79	2.88
Tb	1.00	0.85	—	—	0.34	0.37	0.42	0.32	0.47
Dy	6.44	5.47	—	—	2.31	2.45	2.62	2.14	2.98
Ho	1.38	1.17	—	—	0.50	0.53	0.55	0.47	0.64
Er	4.30	3.58	—	—	1.50	1.59	1.64	1.38	1.87
Tm	0.64	0.51	—	—	0.22	0.23	0.23	0.20	0.26

(Continued)

Table 1: Continued

Yb	4.44	3.45	—	—	1.43	1.55	1.55	1.34	1.77
Lu	0.67	0.53	—	—	0.22	0.23	0.23	0.21	0.27
Hf	4.78	3.14	—	—	0.94	1.01	1.06	0.90	1.22
Ta	0.235	0.149	—	—	0.019	0.022	0.024	0.023	0.030
Pb	5.42	3.22	—	—	1.30	1.40	2.36	1.17	2.79
Th	3.074	1.590	—	—	0.255	0.285	0.832	0.239	0.967
U	1.018	0.541	—	—	0.110	0.156	0.263	0.106	0.323
Isotopes									
$^{87}Sr/^{86}Sr$	0.703718	0.703618	—	—	—	0.703992	0.704038	0.703976	—
(2SE)	*0.000008*	*0.000008*	—	—	—	*0.000007*	*0.000007*	*0.000007*	—
$^{143}Nd/^{144}Nd$	0.512950	0.512974	—	—	—	0.513000	0.512904	0.512996	—
(2SE)	*0.000009*	*0.000007*	—	—	—	*0.000008*	*0.000009*	*0.000007*	—
$^{176}Hf/^{177}Hf$	0.283151	0.283156	—	—	—	0.283167	0.283153	0.283164	—
(2SE)	*0.000007*	*0.000005*	—	—	—	*0.000006*	*0.000005*	*0.000006*	—
$^{206}Pb/^{204}Pb$	18.841	18.839	—	—	—	18.889	18.850	18.890	—
(2SE)	*0.001*	*0.001*	—	—	—	*0.001*	*0.001*	*0.001*	—
$^{207}Pb/^{204}Pb$	15.624	15.624	—	—	—	15.630	15.629	15.630	—
(2SE)	*0.001*	*0.001*	—	—	—	*0.001*	*0.001*	*0.001*	—
$^{208}Pb/^{204}Pb$	38.680	38.673	—	—	—	38.686	38.692	38.685	—
(2SE)	*0.003*	*0.003*	—	—	—	*0.002*	*0.003*	*0.002*	—

Sample ID:	**DR29-1**	**DR29-2**	**DR29-8**	**DR29-23**	**DR29-28**
Latitude(°S)	**34.57**	**34.57**	**34.57**	**34.57**	**34.57**
Longitude(°E)	**179.34**	**179.34**	**179.34**	**179.34**	**179.34**
Depth (m)	**2293**	**2293**	**2293**	**2293**	**2293**
Major elements (XRF) wt %					
SiO_2	51.25	49.50	48.45	48.73	66.13
TiO_2	0.81	0.65	0.35	0.65	0.63
Al_2O_3	16.60	17.65	11.82	17.43	15.37
Fe_2O_3	11.23	10.39	7.95	11.37	5.42
MnO	0.19	0.18	0.14	0.18	0.15
MgO	5.38	6.39	14.19	6.21	1.33
CaO	11.14	12.63	16.06	13.09	4.07
Na_2O	2.58	1.82	0.74	1.75	4.40
K_2O	0.42	0.30	0.15	0.09	1.82
P_2O_5	0.11	0.09	0.06	0.09	0.17
Total	99.70	99.61	99.90	99.59	99.48
Trace elements (XRF) ppm					
V	315.6	302.6	213.7	294.0	57.0
Cr	11.8	57.4	505.5	28.2	6.8
Ni	11.5	32.6	142.6	24.7	5.4
Cu	40.3	149.3	75.0	142.1	22.1
Zn	69.7	72.5	43.5	56.6	78.6
Rb	10.0	5.8	3.9	3.9	47.4
Sr	218.3	191.2	134.6	193.0	192.1
Ba	172.1	157.5	105.2	100.1	623.0
Y	15.5	13.6	6.9	13.2	37.5
Zr	48.5	32.9	15.1	30.2	155.8
Nb	1.0	0.8	0.5	0.7	3.4
Trace elements (ICP-MS) ppm					
	iCAPQ	iCAPQ	iCAPQ		iCAPQ
Sc	25.5	34.9	53.0	—	8.1
Ni	10.5	32.1	133.4	—	0.6
Rb	7.0	4.2	2.6	—	40.6
Sr	189.1	185.6	125.7	—	184.5
Y	12.9	13.2	6.7	—	33.2
Zr	39.8	31.9	13.5	—	139.5
Nb rec	0.76	0.61	0.29	—	3.18
Cs	0.30	0.27	0.12	—	1.49
Ba	141.9	143.9	73.9	—	545.3
La	2.97	2.07	1.34	—	12.51
Ce	7.53	5.51	3.30	—	29.41
Pr	1.14	0.88	0.51	—	4.17
Nd	5.73	4.70	2.66	—	19.19
Sm	1.75	1.58	0.85	—	5.07

(Continued)

Table 1: Continued

Eu	0.70	0.59	0.33	—	1.25
Gd rec	2.20	2.09	1.12	—	5.64
Tb	0.38	0.38	0.20	—	0.96
Dy	2.53	2.52	1.31	—	6.14
Ho	0.55	0.54	0.27	—	1.31
Er	1.63	1.63	0.82	—	4.02
Tm	0.24	0.24	0.11	—	0.59
Yb	1.56	1.57	0.76	—	4.01
Lu	0.24	0.24	0.11	—	0.62
Hf	1.21	1.00	0.46	—	3.91
Ta	0.048	0.034	0.015	—	0.202
Pb	1.23	1.32	0.76	—	4.75
Th	0.493	0.256	0.211	—	2.431
U	0.178	0.107	0.084	—	0.827
Isotopes					
$^{87}Sr/^{86}Sr$	—	0.703834	0.703858	—	0.703721
(2SE)	—	*0.000009*	*0.000007*	—	*0.000009*
$^{143}Nd/^{144}Nd$	—	0.513002	0.512952	—	0.512935
(2SE)	—	*0.000008*	*0.000009*	—	*0.000008*
$^{176}Hf/^{177}Hf$	—	0.283157	0.283132	—	0.283143
(2SE)	—	*0.000005*	*0.000005*	—	*0.000005*
$^{206}Pb/^{204}Pb$	—	18.862	18.867	—	18.844
(2SE)	—	*0.001*	*0.001*	—	*0.001*
$^{207}Pb/^{204}Pb$	—	15.626	15.633	—	15.626
(2SE)	—	*0.001*	*0.001*	—	*0.001*
$^{208}Pb/^{204}Pb$	—	38.686	38.715	—	38.687
(2SE)	—	*0.003*	*0.003*	—	*0.003*

Low-Mg andesites, dacites, rhyolites

The low-Mg andesites are poorly vesiculated fine-grained lavas consisting of clinopyroxene, orthopyroxene, plagioclase, and interstitial magnetites. Ilmenite is observed in most differentiated samples. The groundmasses are mostly composed of plagioclase laths and intergranular pyroxenes. Pyroxenes are normally zoned and less magnesian compared to those of the magnesian andesites (Mg# = 61–75; Fig. S1). This is consistent with the relatively high FeO*/MgO values of the whole-rock compositions (Fig. 4). Plagioclases are normally zoned, showing a higher An content in the core ($An_{53–85}$) than in the rim ($An_{45–69}$).

The dacites are highly vesiculated pumiceous rocks containing clinopyroxene, orthopyroxene, plagioclase, and amphibole with minor magnetite ± ilmenite. The pyroxenes (Mg# = 59–76; Fig. S1) often occur as glomerocrysts with plagioclases. Amphiboles occur as microphenocrysts (<0.4 mm) and show slightly lower Mg#s than the pyroxenes (Mg# = 54–67; Fig. S1). Amphiboles are classified as edenites and magnesiohornblendes of the calcic amphibole group, according to the definition of Leake *et al.* (1997). Plagioclases ($An_{29–60}$; Fig. S1) dominate the phenocrysts. These minerals are generally unzoned to normally zoned, but weakly reverse-zoned grains and altered lithic clasts (~1 mm) rarely appeared. The altered lithic clasts have angular shapes and clear borders with surrounding groundmasses.

Rhyolites have a petrography, mineral assemblages, and mineralogy similar to those of dacites, whereas clinopyroxene is a minor phase in rhyolites. The mafic minerals in the rhyolites tend to have lower Mg#s than those in the dacites when compared with the rim and groundmass compositions (Fig. S1).

Basalts from neighboring cones

Basalts KI1, KI3, and KI4 generally consist of olivine, clinopyroxene, and plagioclase in various modal proportions. Distinct in the magnesian samples (Mg# = 65–78) are the large modal proportions of clinopyroxenes. For example, the most magnesian basalt from KI3 (DR29-8: whole-rock Mg# = 78) contains 11 vol % (excluding vesicles) olivine and 29 vol % clinopyroxene within a poorly vesiculated groundmass. Ca-rich plagioclases are also dominant (17 vol %; $An_{79–97}$; Fig. S1). The olivines show bimodal forsterite contents ($Fo_{76–82}$ and $Fo_{86–90}$; Fig. S1) that are lower than the equilibrium olivine compositions with the whole-rock composition ($Fo_{93–95}$; Fig. S1). This sample is deemed to be a cumulate of mafic minerals because it contains no olivine in equilibrium with the whole-rock composition. The most magnesian basalt from KI4 (DR28-25: whole-rock Mg# = 72) contains 17 vol % olivine and 28 vol % clinopyroxene and has highly vesiculated groundmass. Unlike DR29-8, plagioclase is in a minor phase (<1 vol %; $An_{82–90}$). In DR28-25, most magnesian olivine (Fo_{92}) is in equilibrium with the whole-rock compositions (Fig. S1), and the olivines and clinopyroxenes show a wide range of compositions ($Fo_{80–92}$ for olivine and Mg# = 79–94 for clinopyroxene). Chromian spinels are included in the forsteritic olivines ($Fo_{90–92}$) and have high Cr# (79–85).

Other basalts from KI1, KI3, and KI4 are less magnesian (Mg# = 48–61) and less porphyritic (<15 vol % mafic minerals) than the magnesian basalts but often contain olivine and clinopyroxene megacrysts up to ~5 mm. The olivine megacrysts show higher Fo contents than those in equilibrium with the whole-rock compositions (Fig. S1), indicating their xenocrystic origin.

Basalts from the unnamed cone consist mainly of olivine with minor clinopyroxene and plagioclase. Despite their primitive

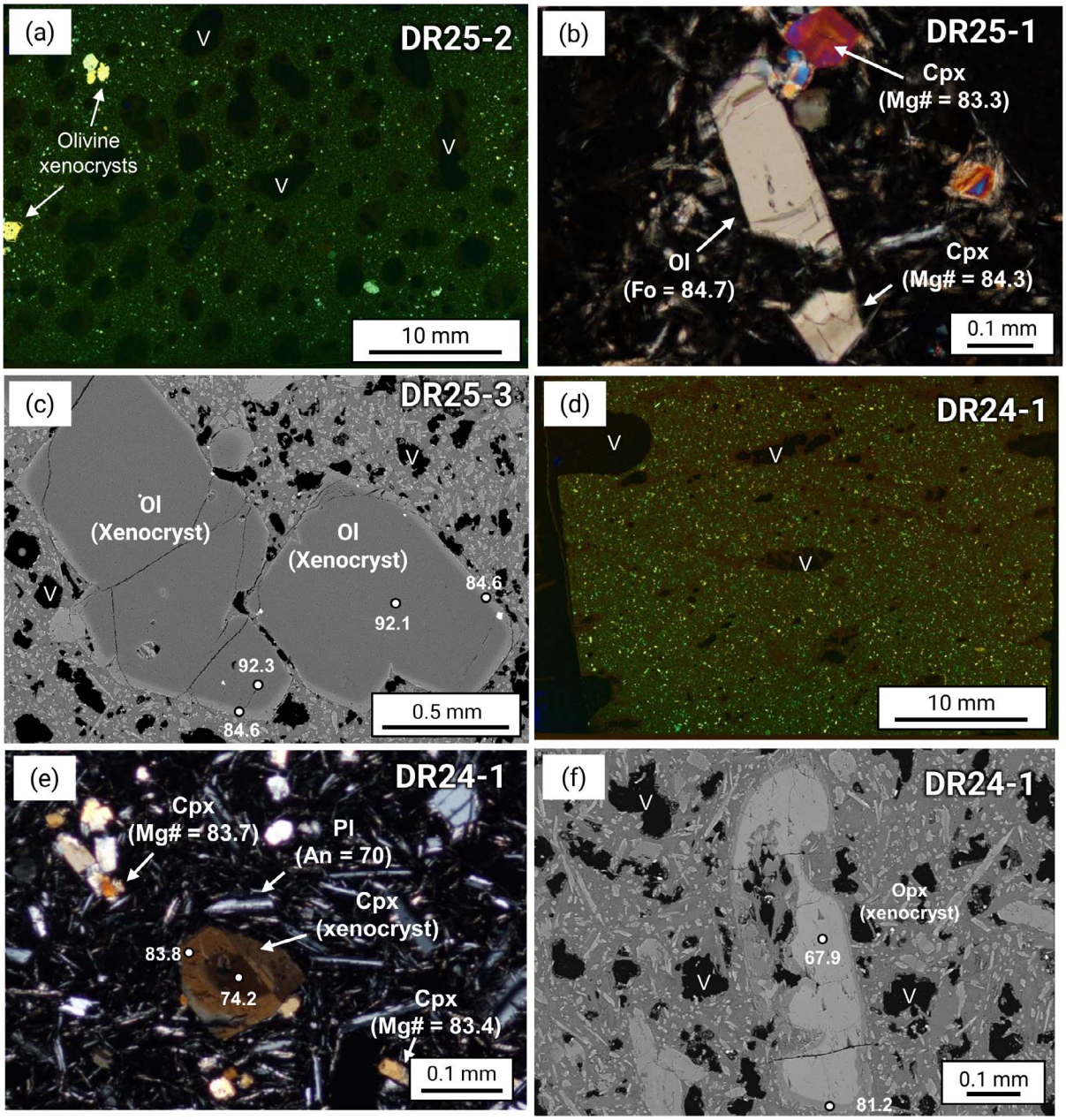

Fig. 5. Photographs of thin sections for the magnesian andesites from the Kibblewhite Volcano. (a) Sample DR25-2 under cross-polarized lights. The sparse relatively large crystals (~1 mm) are olivine xenocrysts (Fo_{92}). 'V' denotes vesicle. (b) Olivine and clinopyroxene microphenocrysts in the magnesian andesite (DR25-1). (c) Back-scattered electron (BSE) image of olivine xenocrysts in sample DR25-3. Forsteritic olivine xenocrysts (Fo_{92}) are surrounded by thin rims (Fo_{85}) that have similar compositions to groundmass olivines (Fo_{85}). (d) Sample DR24-1 under cross-polarized light. This sample is composed of clinopyroxene + plagioclase microphenocrysts and poorly vesiculated lavas compared to magnesian andesites collected from DR25. Reversely zoned clinopyroxene xenocryst and groundmass clinopyroxenes in sample DR24-1 under cross-polarized light. (f) BSE image of dissolved orthopyroxene xenocryst (only one grain is observed in the thin section) in sample DR24-1, which has a thin, bronzite rim (Mg# = 81.2). Open circles indicate the analyzed points by EPMA (not representative of beam size), and the associated numbers indicate the Mg#s (= 100 Mg/[Mg + Fe]).

whole-rock compositions (whole-rock Mg# = 63–68), they are less porphyritic (<3 vol % olivine) than the magnesian basalts from the other cones. Chromian spinels are included in the olivine phenocrysts ($Fo_{86–90}$) and show lower Cr numbers (50–60) than basalts from KI4.

Nickel content in olivine

The olivine microphenocrysts of the magnesian andesites have a limited range of NiO contents (0.14–0.19 wt % NiO), which positively correlate with the Fo contents (Fig. 6a). These NiO contents are higher than those in the olivines in the basalts at the same Fo content (Fig. 6a). The olivine xenocrysts in the magnesian andesites show various NiO contents despite the limited Fo contents (0.18–0.36 wt % NiO at $Fo_{91–93}$).

Olivines in the basalts from KI1, KI3, and KI4 show Fo contents comparable to those of mantle peridotites ($Fo_{90–92}$), but the NiO contents are notably lower (<0.2 wt % NiO; Fig. 6a). The olivines of basalts from the unnamed cone are characterized by higher

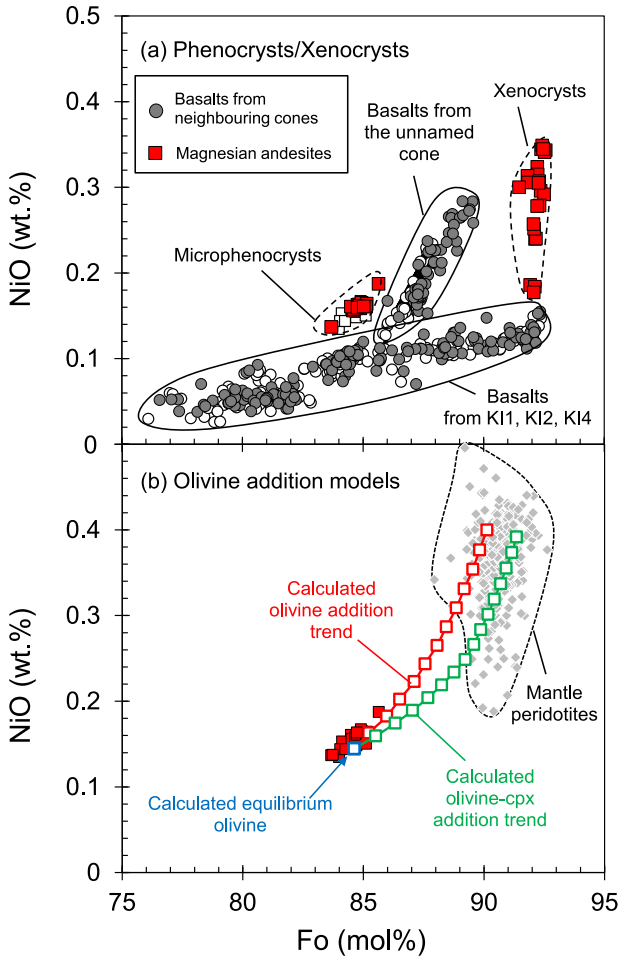

Fig. 6. Variations of NiO versus forsterite content (Fo: 100 Mg/[Mg + Fe]) for olivines in volcanic rocks from the Kibblewhite Volcano. (a) Olivines in the magnesian andesites and basalts from neighboring cones. The filled and open symbols indicate the core and rim compositions, respectively. (b) Estimation of olivine and olivine + clinopyroxene addition trends for the magnesian andesites. Open blue square is the calculated olivine composition in equilibrium with the whole-rock composition of sample DR25-1. Red and green lines with open squares indicate calculated olivine and olivine + clinopyroxene addition trends for the magnesian andesite, respectively. Markers on the addition trends denote a 1% increment in addition. Diamonds show olivines from abyssal peridotites collected from worldwide mid-ocean ridges (Warren, 2016) and forearc peridotites from the Tonga arc (Birner *et al.*, 2017).

NiO contents than the other basalts at the same Fo content and a positive correlation between the NiO and Fo contents (Fig. 6a).

Major and trace elements

Fig. 7 shows the SiO_2 variation diagrams for the volcanic rocks from the Kibblewhite Volcano. Those from the main cone have moderate K_2O concentrations (0.8–2.2 wt %) falling in the medium K suite of Gill (1981), whereas basalts from the neighboring cones have a low-K character (<0.8 wt % K_2O). Variations in major elements and compatible trace elements (e.g. Cr and Ni) in the volcanic rocks from the Kibblewhite Volcano coincide with those in the lavas from the Kermadec arc front. The magnesian andesites have lower TiO_2, Al_2O_3, and FeO* contents and higher MgO, CaO, Cr (not shown), and Ni contents at a given SiO_2 content than the low-Mg andesites.

The major element composition of the quenched glass from magnesian andesite (DR25-1) is shown in Fig. 7. Although the glass has major elemental characteristics similar to its whole-rock composition, it shows slightly higher SiO_2, Al_2O_3, and total alkali contents and lower TiO_2, FeO*, MgO, and CaO contents.

On a normal mid-ocean ridge basalt (N-MORB; Sun & McDonough, 1989)-normalized trace element diagram (Fig. 8), all samples from the Kibblewhite Volcano show slightly depleted Nb and Ta relative to heavy REE. Spikes of large ion lithophile elements (Rb, Ba, K, Pb, and Sr) are recognized in all samples in the diagram, indicating that slab-derived components contributed to their sources (Elliott, 2003).

In the chondrite (McDonough & Sun, 1995)-normalized REE diagrams (Fig. 9), the magnesian andesites show light REE (LREE)-enriched patterns, which distinguish them from the low-Mg andesites that show a relatively flat REE pattern. Dacites and rhyolites have LREE-enriched patterns parallel to the patterns of magnesian andesites. The basalts show variable REE patterns, ranging from LREE depleted to LREE enriched (Fig. 9). Negative anomalies of Eu compared adjacent REEs (Sm and Gd) are commonly observed in dacites and rhyolites.

Sr–Nd–Hf–Pb isotopes

The Sr–Nd–Hf–Pb isotope compositions of the volcanic rocks from the Kibblewhite Volcano are plotted within the range of the Kermadec arc-front lavas (Fig. 10). Data from this study are consistent with published data for the Kibblewhite Volcano (Gill *et al.*, 2021; Hauff *et al.*, 2021), and isotopic compositions of the basalts varied more than the andesites, dacites, and rhyolites (Fig. 10).

DISCUSSION

Influence of crystal accumulation and crustal contamination

Some primitive andesites observed in the subduction zones have been produced by magma mixing or accumulation of mafic minerals. Primitive andesites from Mt. Shasta have the following petrographic features that are suspected to be derived from magma mixing or crustal contamination: (1) high-Mg# olivine (and orthopyroxene) xenocrysts and (2) low-Mg# (65–72) clinopyroxene and orthopyroxene xenocrysts (Streck *et al.*, 2007; Streck & Leeman, 2018). The magnesian andesites from the Kibblewhite Volcano have petrographic features similar to those of the Mt. Shasta andesites, indicating that they were affected by such secondary modification processes during ascent.

However, we do not consider that the magnesian andesites were primarily generated by magma mixing or crustal contamination processes for two reasons. First, the magnesian andesites from the Kibblewhite Volcano are nearly aphyric and composed of olivine and clinopyroxene microphenocrysts in equilibrium with whole-rock compositions, which is inconsistent with the magma mixing origin. Magnesian andesites produced by mixing mafic and felsic end-member magmas are known to be porphyritic and contained reversely zoned olivine and pyroxenes (Ohba *et al.*, 2007). Olivine xenocrysts in the Kibblewhite magnesian andesites are rare (<2 vol %) and are much too low in abundance to change the magma composition from low-Mg to magnesian. An exception is DR24-1, which contains reversely zoned clinopyroxene and orthopyroxene (Fig. 5e), which could have been caused by the mixing of the magnesian andesite with felsic magma. Second, the quenched groundmass glass from the magnesian andesites shows major elemental characteristics similar to those of the whole-rock magnesian andesites (Fig. 7). If magnesian andesites resulted from the incorporation of mafic minerals, the groundmass glass should have a more differentiated composition

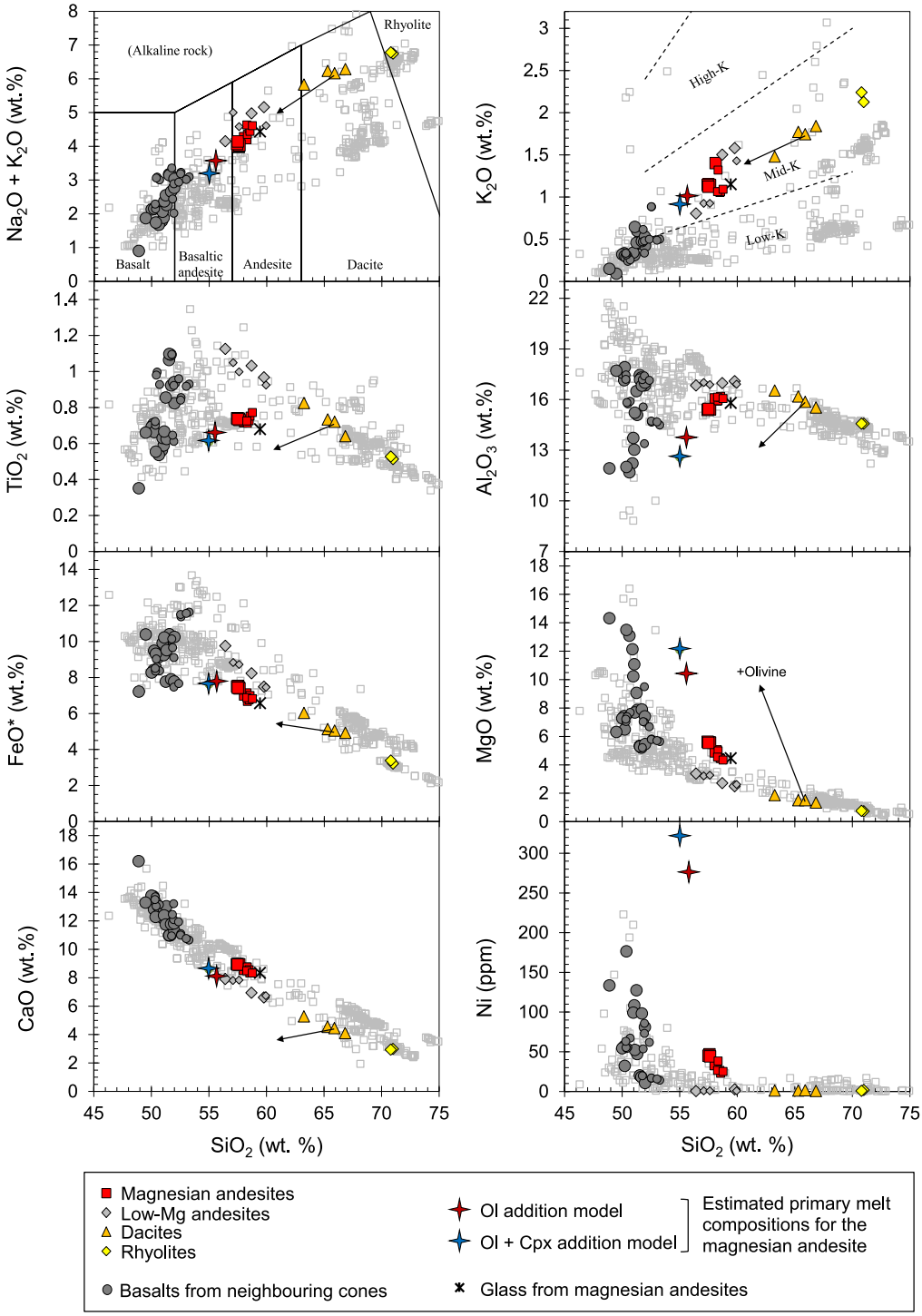

Fig. 7. SiO_2 variation diagrams for major and compatible elements in volcanic rocks from the Kibblewhite Volcano and neighboring cones. Discrimination boundary lines are from Le Maitre (2002) in the total alkali–silica ($Na_2O + K2O–SiO_2$) diagram and Gill (1981) in K_2O- SiO_2 diagram. Small symbols are the published data for Kibblewhite Volcano (Hauff *et al.*, 2021). Open gray squares are volcanic rocks from the Kermadec arc front (data sources are the same as in Fig. 4). Red and blue crosses show the primary melt compositions for the magnesian andesite, estimated by the olivine addition and olivine + clinopyroxene addition models, respectively. Arrows represent inferred compositional changes in dacite when it incorporates olivine crystals.

than the bulk rock composition. This strongly suggests that the olivine and clinopyroxene xenocrysts contained in the magnesian andesites do not significantly affect whole-rock composition. Based on these observations, we consider that the magnesian andesites from the Kibblewhite Volcano are not a product of magma mixing or the accumulation of mafic minerals.

Estimation of primary melt compositions

The Kibblewhite magnesian andesites are not in equilibrium with mantle olivine (Fig. 6) and resulted from olivine ± clinopyroxene fractionation from the primary melts because they contain microphenocrysts of olivine and clinopyroxene that are in equilibrium with the whole-rock composition (Fig. 5b). Therefore,

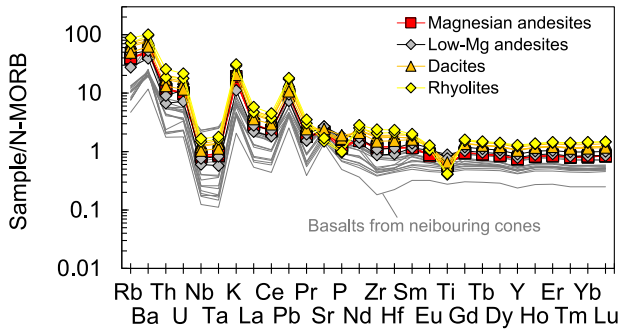

Fig. 8. Normal-type mid-ocean ridge basalt-normalized trace element patterns for volcanic rocks from the Kibblewhite Volcano. Gray lines show basalts from neighboring cones. Normalizing values are from Sun & McDonough (1989).

the primary melt compositions of the magnesian andesites were estimated using the olivine addition model proposed by Tamura *et al.* (2014) (Fig. 6b). In the model, the equilibrium Fo and NiO contents in olivine with the whole-rock composition were calculated, and the calculated equilibrium olivine was iteratively added to the whole-rock composition of sample DR25-1 in 1% steps until the NiO content of the calculated equilibrium olivine was in equilibrium with the mantle peridotites (~0.4 wt % NiO). In addition, an olivine + clinopyroxene addition model was used to investigate the effects of clinopyroxene fractionation (Fig. 6b). In this model, clinopyroxene (Mg# = 87) was simultaneously added to the calculated equilibrium olivine in a 1:1 ratio until the calculated olivine composition had Fo_{89}. The ratio of the added olivine to clinopyroxene was assumed to be the modal proportion of the microphenocryst phases in the magnesian andesites. The composition of the clinopyroxene microphenocrysts in sample DR25-3 was used for the clinopyroxene addition.

The estimated primary melt composition after the addition of 12 wt % equilibrium olivine is andesitic in composition (55.8 wt % SiO_2, 10.3 wt % MgO, Mg# = 70) and in equilibrium with $Fo_{90.1}$ olivine (Table 2). When 6 wt % clinopyroxene was added, the addition of 15 wt % olivine was required to produce primary melts (55.0 wt % SiO_2, 12.1 wt % MgO, Mg# = 74). The total amount of olivine added in the olivine + clinopyroxene model was larger than that in the olivine model because the addition of clinopyroxene does not significantly increase the Ni content in the melts (Fig. 6b). The olivine + clinopyroxene addition model estimated a more magnesian primary melt composition in equilibrium with the $Fo_{91.4}$ olivine, but the melt was still andesitic. Thus, the addition of clinopyroxene increases the Mg# in the estimated primary melt but does not significantly affect its SiO_2 content. If we assumed greater amounts of clinopyroxene, the estimated primary melts would be more magnesian and in equilibrium with more forsteritic olivine ($Fo_{\sim 92}$); however, the SiO_2 content remained at 54–55 wt %. Xenocrystic olivines have $Fo_{\sim 92}$; thus, the primary melts of the magnesian andesites should have been andesitic.

We compared the estimated primary melts of the Kibblewhite magnesian andesites with the primitive basaltic and andesitic magmas previously observed in subduction zones (Fig. 11). The two types of primitive andesites, HMAs ('type-2 low-Ca boninites' as defined by Crawford *et al.*, 1989) and boninites ('type-1 low-Ca boninites') are shown in Fig. 11. High-Mg# andesites are distinguished from boninites by their higher TiO_2, Al_2O_3, and total alkali contents. The estimated primary melts of the magnesian andesites have similar CaO and CaO/Al_2O_3 to the HMAs and boninites but are distinguished from the primitive basalts. The TiO_2 and total alkali contents of the estimated primary melts are similar to those of the HMAs, which are much higher than those of the boninites. This suggests that the magnesian andesites were differentiated from primary melts that have geochemical features similar to those of HMAs, rather than boninites. Hereafter, we refer to the estimated primary melt compositions of the magnesian andesites as 'Kibblewhite HMA'.

Origin of the 'Kibblewhite HMA'

There are different pathways for the generation of HMAs in subduction-zone environments. However, it is impossible to distinguish all the processes in the mantle based on the chemical compositions alone. Thus, we discuss the origin of the Kibblewhite HMA while focusing on three major models proposed in previous studies.

(1) Interaction of slab melts with mantle peridotites

The interaction between partial melts from the subducting slab and sub-arc mantle peridotites is an important process in the generation of HMAs (Defant & Drummond, 1990; Yogodzinski *et al.*, 1995, 2014; Tatsumi & Hanyu, 2003). However, we consider this process unsuitable for explaining the origin of Kibblewhite HMA for two reasons. First, there is no evidence that slab-derived melt contributed to the source. For example, the HMAs observed in the western Aleutian arc are characterized by high Sr/Y (50–350) and La/Yb (8–35) ratios. These geochemical features have resulted from the re-equilibration of rhyodacitic melts from the subducting slab, called 'adakitic melts', with the overriding mantle wedge (Yogodzinski *et al.*, 1995, 2014; Kelemen *et al.*, 2003*b*). The magnesian andesites from the Kibblewhite Volcano show comparatively low Sr/Y (8–10) and La/Yb (2.7–3.0), which precludes a significant contribution from 'adakitic melts' in their source.

The isotopic compositions also provide evidence that slab melt–mantle interaction is unlikely to produce magnesian andesites. If the magnesian andesites were generated by the interaction between the slab melts and the wedge mantle, the isotopic compositions of the magnesian andesites should have been distinguished from those of the coeval basalts and have isotopic characteristics similar to those of the subducting slab components. This is because slab melts have much higher concentrations of the trace elements of interest (Sr, Nd, Hf, and Pb) than mantle wedge peridotites (Tatsumi & Hanyu, 2003). It has been suggested that the mantle source of the Kermadec arc-front volcanoes is affected by subducting sediments (Todd *et al.*, 2010, 2011) or the subducted Hikurangi Plateau with its seamounts (Timm *et al.*, 2014; Hoernle *et al.*, 2021). Thus, slab melts are expected to have isotopic compositions reflecting the mixing array between these subducting components. However, the isotopic compositions of the magnesian andesites are similar to those of the coeval basalts and other Kermadec arc-front lavas (Fig. 10). This indicates that the contribution of slab-derived melts was not the main factor determining the silica content of the primary melts. The magnesian andesites have the Sr-Nd-Pb isotope compositions overlapped the field of the Hikurangi Plateau but show high $^{176}Hf/^{177}Hf$ values that are comparable to those of the depleted N-MORBs (Fig. 10). Hafnium behaves as an immobile element in slab-derived fluids owing to the residual zircon in the slab (Tollstrup & Gill, 2005; Todd *et al.*, 2010; Hirai *et al.*, 2018). Thus, the high $^{176}Hf/^{177}Hf$ values, similar to the depleted N-MORB in the magnesian andesites, may be explained by the contribution of slab-derived fluids to the source mantle

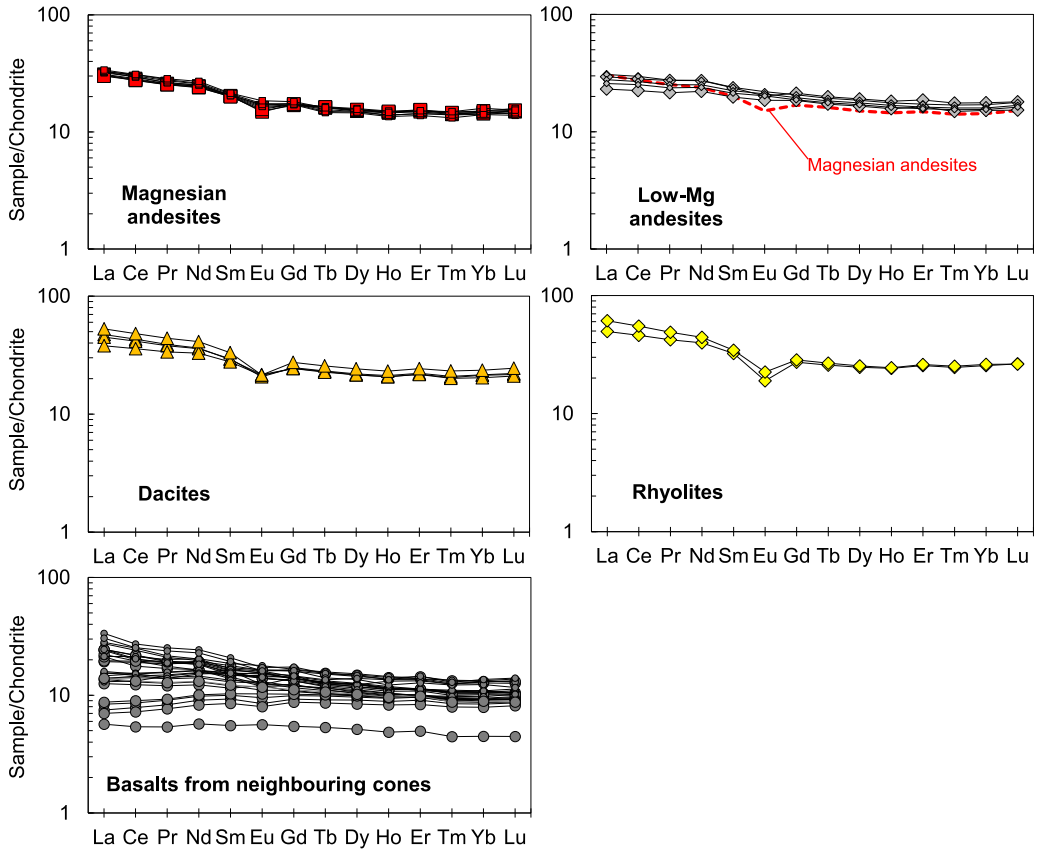

Fig. 9. C1 chondrite-normalized REE patterns for the volcanic rocks from the Kibblewhite Volcano and the basalts from neighboring cones. Small symbols are the published data for Kibblewhite Volcano (Hauff *et al.*, 2021). Normalizing values are from McDonough & Sun (1995).

rather than the slab melt–mantle interaction. However, the Nd-Hf isotope field of the Hikurangi Plateau shown in Fig. 10 may have been underestimated because of insufficient Hf isotope data for them. Thus, the most robust evidence to support this origin may be to discover a magma with an adakitic signature as that of other arcs (Yogodzinski *et al.*, 2015), but no adakitic magma is known in the Kermadec arc.

(2) Melting of a hybridized peridotite/pyroxenite source in mantle wedge

High-Mg# andesites from the central Mexican Volcanic Belt are interpreted to have resulted from the melting of a hybridized peridotite-pyroxenite source, which was formed by the interaction between slab-derived silicic melts and the lithospheric mantle (Straub *et al.*, 2008, 2014). A similar case was reported for the Kamchatka Arc (Nishizawa *et al.*, 2017). These HMAs are characterized by olivine phenocrysts with extremely high Ni content (~0.6 wt % NiO at Fo_{90}). Because the melting of pyroxenite produced melts with high Ni content (Sobolev *et al.*, 2005), Straub *et al.* (2008, 2011, 2014) proposed that the HMAs of the Mexican Volcanic Belt are produced by the melting of a peridotite sub-arc mantle interspersed with pyroxenite veins.

We consider it unlikely that Kibblewhite HMAs were produced by the melting of such hybridized peridotite/pyroxenite for two reasons. First, such high-Ni olivines are not observed in the Kibblewhite magnesian andesites. Olivine xenocrysts in the magnesian andesites, which could have originated from disaggregated mantle xenoliths, have NiO contents consistent with peridotites (0.18–0.36 wt % NiO at $Fo_{91–93}$; Fig. 6).

Table 2: Estimated primary melt compositions for the magnesian andesite (DR25-1) by olivine addition (Ol) and olivine and clinopyroxene addition (Ol + Cpx) models

Addition model:	Ol	Ol + Cpx
Added Ol:	12%	15%
Added Cpx:		6%
Calculated melt composition		
SiO_2 (wt %)	55.8	55.0
TiO_2	0.66	0.61
Al_2O_3	13.7	12.6
FeO*	7.7	7.6
MnO	0.17	0.16
MgO	10.3	12.1
CaO	8.0	8.6
Na_2O	2.5	2.3
K_2O	1.00	0.90
P_2O_5	0.13	0.12
Mg#	70.4	73.9
CaO/Al_2O_3	0.58	0.68
Equilibrium olivine composition		
Fo (mol %)	90.1	91.4
NiO (wt %)	0.40	0.39

Another reason is that this model cannot account for the major element compositions of the Kibblewhite HMAs. The melting of secondary pyroxenites, formed by slab melt–mantle interactions, produces dacitic melts with high Mg# (Rapp *et al.*, 1999, 2010; Fig. 11). The major elemental compositions of the Mexican

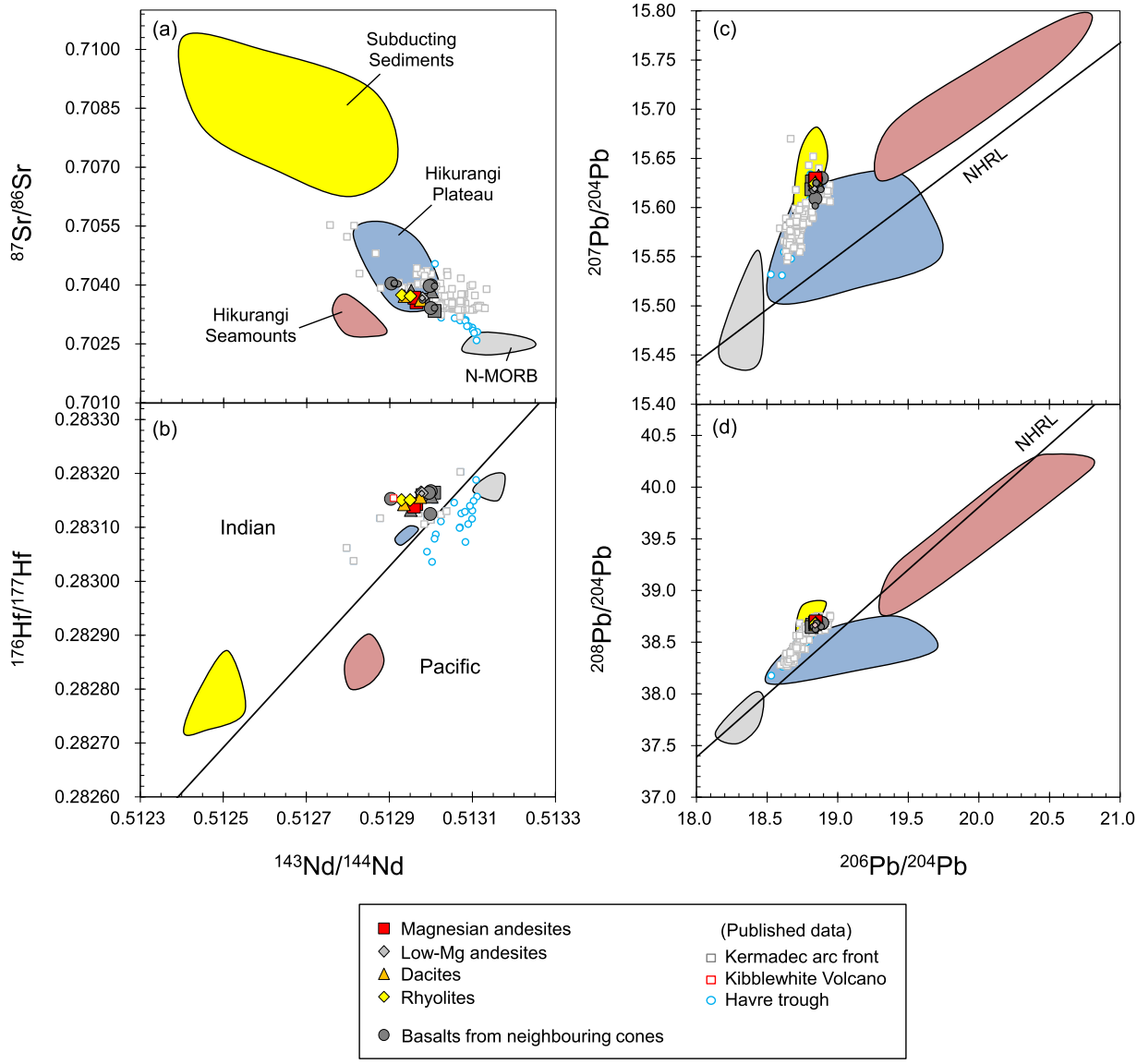

Fig. 10. Whole-rock Sr–Nd–Hf–Pb isotope ratios for the volcanic rocks from the Kibblewhite Volcano and neighboring cones. Pacific–Indian-type mantle discrimination boundary line in the Nd-Hf isotope space is after Pearce *et al.* (2007). Northern hemisphere reference lines (NHRL) in Pb isotope spaces are based on Hart *et al.* (1986). Open blue circles and yellow triangles are the volcanic rocks from the Havre trough (Ngatoro rift and Ngatoroirangi rift; Todd *et al.*, 2011) and the Rumble V ridge (Todd *et al.*, 2010), respectively. The data of normal-type mid-ocean ridge basalts (N-MORB) from the Eastern Pacific Rise, shown only with Nb/Yb <1.0 to exclude samples having anomalously enriched compositions, were downloaded from the PetDB Database (www.earthchem.org/petdb) on 19 July 2021, using the following parameters: feature name = Spreading Center: East Pacific Rise and rock classification = basalt. All references of the N-MORB data are given in supplementary Table S4. Small symbols are the published data for Kibblewhite Volcano (Hauff *et al.*, 2021). The compositions of subducting slab components to the Kermadec arc are shown as follows: subducting sediments (Gamble *et al.*, 1996; Turner *et al.*, 1997; Ewart *et al.*, 1998; Todd *et al.*, 2010), Hikurangi plateau (Mortimer & Parkinson, 1996; Hoernle *et al.*, 2010; Timm *et al.*, 2014), and Hikurangi seamounts (Hoernle *et al.*, 2010).

HMAs could be reproduced by mixing pyroxenite-derived dacitic melts and peridotite-derived basaltic melts in appropriate proportions (Straub *et al.*, 2011). However, pyroxenite-derived dacitic melts have low MgO and FeO contents because olivine did not participate in the melting process (Fig. 11). Thus, if pyroxenite melting is important for the generation of Kibblewhite HMAs, the MgO and FeO contents would be lower than those in the peridotite-derived melts. Indeed, the Mexican and Kamchatka HMAs, which have been implicated in pyroxenite melting, are characterized by low contents of these elements (6–8 wt % MgO; 5–7 wt % FeO) (Straub *et al.*, 2008, 2011, 2014; Nishizawa *et al.*, 2017). The Kibblewhite HMAs, however, have higher MgO and FeO contents (10–12 wt % MgO; 7.6–7.7 wt % FeO) at a similar Mg#, resembling the values of peridotite-derived melts rather than pyroxenite-derived melts. We believe that this is not because of the method of estimating the Kibblewhite HMAs as the addition of olivine and clinopyroxene did not significantly change the FeO content in the melts (Fig. 11). In addition, if pyroxenite-derived melts contributed to the source, we underestimated the amount of olivine added to the melts because pyroxenite-derived melts should have a high Ni content. As more olivine is added, the MgO content of Kibblewhite HMAs increases. This compositional change is opposite to the contribution of the pyroxenite-derived melts. Therefore, we conclude that the contribution of the pyroxene-derived melt to the Kibblewhite HMAs was minimal or absent.

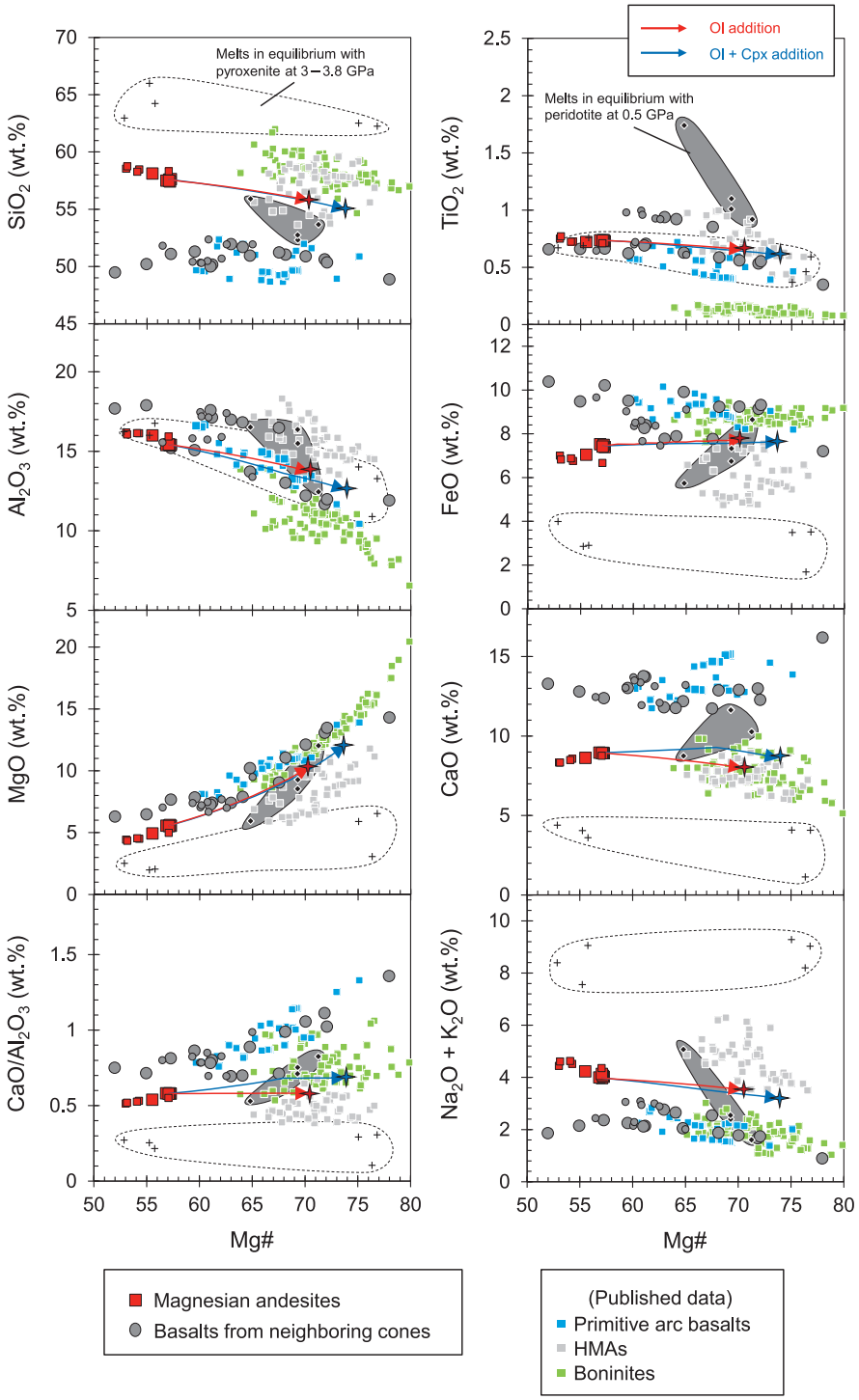

Fig. 11. Comparison of representative major element compositions of the estimated primary melt compositions for the magnesian andesite with primitive arc magmas, using Mg# as a proxy for differentiation. Red and green arrows indicate estimated olivine and olivine + clinopyroxene addition trends, respectively. Red and blue crosses show the primary melt compositions for the magnesian andesite, estimated by the olivine addition and olivine + clinopyroxene addition models, respectively. Basalts from the neighboring cones are also shown for comparison. Small symbols are the published data for Kibblewhite Volcano (Hauff *et al.*, 2021). Data sources for primitive arc basalts (Vanuatu arc: Barsdell, 1988; Barsdell & Berry, 1990; Mariana arc: Tamura *et al.*, 2014), for low-Ca boninites (Ogasawara islands: Umino, 1986; Taylor *et al.*, 1994; Kanayama *et al.*, 2012), and for HMAs (Kamchatka: Bryant *et al.*, 2011; Nishizawa *et al.*, 2017; SW Japan: Tatsumi, 1982; Taupo Volcanic Zone: Heyworth *et al.*, 2007; Cascade: Baker *et al.*, 1994; Grove *et al.*, 2002; Ruscitto *et al.*, 2011; Central Mexican Volcanic Belt: Blatter & Carmichael, 1998; Straub *et al.*, 2014; Western Aleutian: Yogodzinski *et al.*, 1994). Crosses and diamonds represent the experimental melts in equilibrium with pyroxenite at 3.0–3.8 GPa (Rapp *et al.*, 1999, 2010) and peridotite at 0.5 GPa (Kushiro, 1996), respectively.

Recently, Bowman & Ducea (2023) proposed that crustal thickness in subduction zones was proportional to the degree of contribution of pyroxenite-derived melts. This also suggests that a significant contribution of pyroxenite-derived melts to the Kibblewhite HMAs is unlikely because the Kermadec arc is one of the arcs that have the thinnest crusts worldwide.

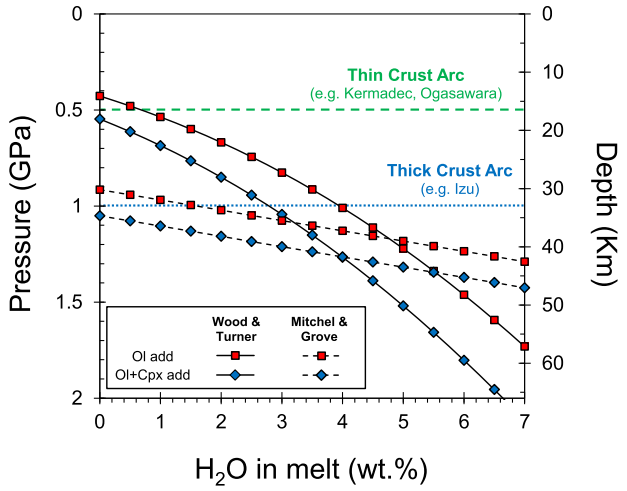

Fig. 12. Estimated pressure conditions for the Kibblewhite HMAs. The calculations were performed using the models of Wood & Turner (2009) and Mitchell & Grove (2015) with the assumption of 0–7 wt % H_2O in the melts. The compositions used for the calculation are shown in Table 2. The horizontal broken and dotted lines represent the depths of the crust–mantle boundaries beneath the oceanic arcs that have thin and thick crusts, respectively. A depth of 33 km corresponds to 1.0 GPa. The intersection of graphs drawn by the two models suggests that the Kibblewhite HMAs were produced at 1.1–1.3 GPa and contained 3.2–5.5 wt % H_2O.

(3) Melting of sub-arc mantle under low-pressure conditions

Regardless of slab melting, melting of the uppermost mantle can directly produce HMAs. Experiments have shown that the following factors increase the SiO_2 content in peridotite-derived melts: (1) the presence of H_2O (Kushiro, 1969; Gaetani & Grove, 1998), (2) low melting pressures (Hirose & Kushiro, 1993; Walter & Presnall, 1994; Kushiro, 1996), and (3) high alkali content (Hirschmann *et al.*, 1998) and a high degree of undersaturation in clinopyroxene (Kushiro, 1972; Wood & Turner, 2009). In particular, the experimental melts from the peridotites drastically change from basaltic to andesitic below 1 GPa (see Fig. 2a in Wood, 2004, for example). Therefore, Grove & Till (2019) proposed that it is possible to directly produce HMAs by melting the uppermost portions of the mantle wedge in subduction zones.

To investigate this model, we estimated the generation conditions of Kibblewhite HMAs using geobarometers developed by Wood & Turner (2009) and Mitchell & Grove (2015). These geothermometers can estimate the melt temperature and pressure conditions from the melt composition based on experimental data and can also be applied to HMA compositions. Importantly, the H_2O content in melts affects the calculated pressures, but it is unclear how much water Kibblewhite HMAs contained. Thus, we assumed the water content and integrated the two barometers to estimate the H_2O content and pressure conditions of the Kibblewhite HMAs. The assumed water contents were 0–7 wt % H_2O, which is a possible range of the known HMAs (Wood & Turner, 2009). The calculated pressures for the Kibblewhite HMAs are shown in Fig. 12. The pressures calculated by both methods increased with increasing water content, but the pressure calculation by the method of Wood & Turner (2009) was more sensitive to water content. Combining the two methods, the intersection of graphs suggests that the Kibblewhite HMAs were produced at 1.1–1.3 GPa and contained 3.2–5.5 wt % H_2O (Fig. 12). If the pressure conditions and water contents for the Kibblewhite HMAs were in this range, the calculated temperatures as per the method of Mitchell & Grove (2015) ranged from 1140 to 1230°C.

The estimated generation conditions are realistic for the Kermadec arc. We emphasize the importance of crustal thickness, as suggested by Tamura *et al.* (2016). The crustal thickness between arc-front volcanoes of the Kermadec arc, ranging from ~9 to 12 km (Bassett *et al.*, 2016; Fig. 2), corresponds to pressures of ~0.5 GPa in the uppermost mantle wedge. The estimated temperature and pressure conditions imply that the hot region (~1200°C) that produced Kibblewhite HMAs laid ~30 km below the crust–mantle boundary of the Kermadec arc (Fig. 13). If these generation conditions are applied to an arc with a thick crust (~30 km) such as the Izu arc, there would be a hot region just below (<10 km) the crust–mantle boundary (Fig. 13). This is not realistic because the estimated temperatures at crust–mantle boundaries for subduction zones were generally 500–800°C (Syracuse *et al.*, 2010). Based on the geothermal gradient, even if the crust was thick, it should be considered that the hot region is located ~30 km below the crust–mantle boundary. If so, in the arc with thick crust, the hot region would exist at depths that HMAs could not occur (~60 km, 1.5–2.0 GPa; Fig. 13), and mantle melting may have produced primary basaltic melts. Thus, the generation of HMAs is impossible when the crust was thicker than ~30 km. In fact, olivine-saturated magnesian andesites are known at the Sumisu Volcano in the Izu Arc, but they are considered to have been produced by the remelting of HMAs that solidified in the crust in the past (Shukuno *et al.*, 2006). This also suggests that even if only primary basaltic magmas are produced beneath the present Izu arc, primitive andesitic magmas were generated when the crust of the Izu arc was still thin, as in the present Kermadec arc (Tamura & Tatsumi, 2002; Tamura *et al.*, 2016). In contrast, Tamura *et al.* (2019) studied olivine-saturated andesites from the active Nishinoshima Volcano in the Ogasawara Arc, where the crust was approximately 20 km thick, and concluded that these andesites were derived from primitive andesitic melts produced by the low-pressure melting of the sub-arc mantle. Thus, we also believe that the thin crust of the Kermadec arc is important for the origin of Kibblewhite HMAs.

For these reasons, we consider that the origin of the Kibblewhite HMA could best be explained by the melting of an uppermost hydrous mantle source below the volcano.

Implications for the magma genesis of the Kermadec arc

Kibblewhite HMAs may be one of the primary magma types in the Kermadec arc. The discovery of the HMAs gives a new perspective to the magma genesis of the Kermadec arc. The origin of the silicic magmas in the Kermadec arc has been discussed between anataxis of amphibole-facies basaltic lower crust (Smith *et al.*, 2003*a*, 2003*b*, 2006, 2010) and fractional crystallization of basaltic magmas (Haase *et al.*, 2011; Barker *et al.*, 2013). These studies, however, are all based on basaltic source materials. The Kibblewhite HMAs suggest that the genesis of silicic magma in the Kermadec arc needs to be discussed from a wider range of source material composition. Indeed, the dacites and rhyolites in the Kibblewhite Volcano may have resulted from fractional crystallization of the magnesian andesites (Hirai and Tamura, in preparation).

In the Kermadec arc, however, basalts and dacites dominate, and andesites are relatively rare (Smith *et al.*, 2003*b*; Wright *et al.*, 2006). Therefore, it may still be difficult to generalize the generation of HMAs on the Kermadec arc from the discovery of the Kibblewhite HMAs alone. We suspected that primitive andesitic magmas are rare in the Kermadec arc because of a sampling bias.

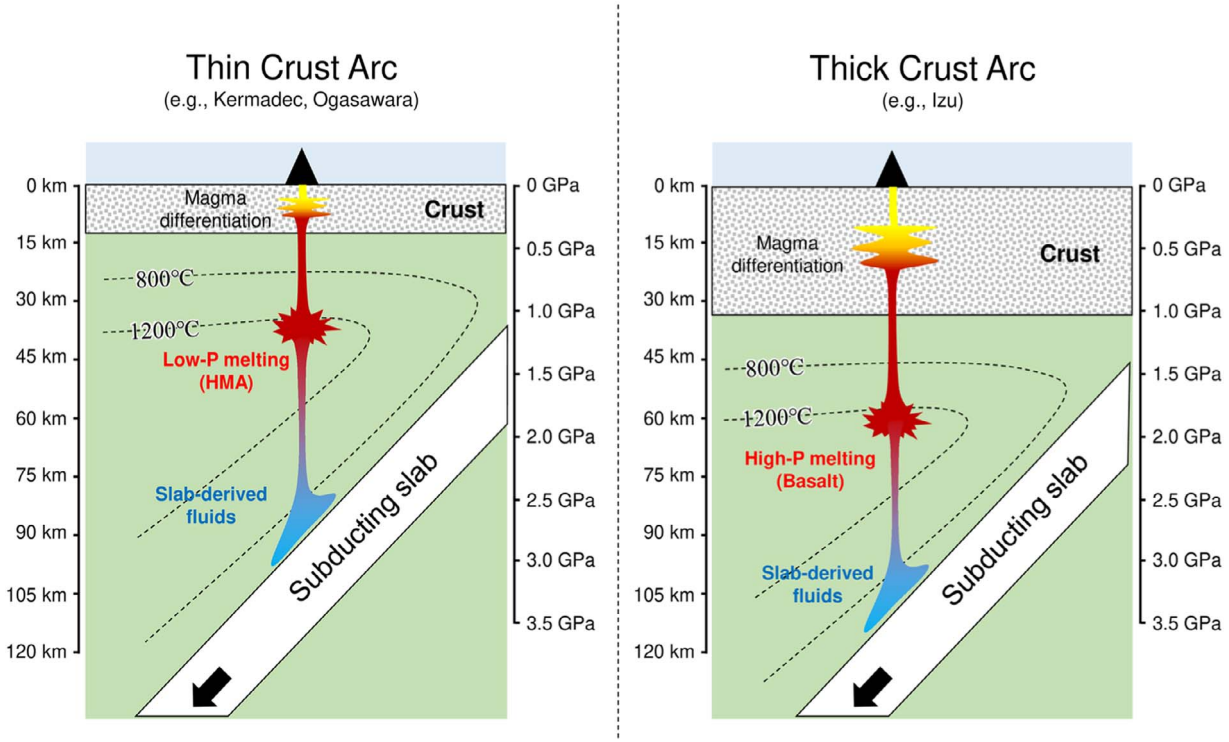

Fig. 13. Schematic illustration showing that the depth (pressure) of primary magma generation varies with the crustal thickness. Approximately 30 km beneath the arc that has thin crust, a hot region (~1200°C) that produces primary melts may be located. Besides the influence of water from the slab-derived fluids, under such temperature and pressure conditions, the primary melt composition will be HMA. In contrast, if the arc has thick crust, the hot region should be at deeper (~60 km; ~2.0 GPa), and the primary melt compositions will be basaltic.

Tamura *et al.* (2014) discovered primitive basalts at the submarine flank of the Pagan volcano in the Marana arc but found only differentiated basalts (<8 wt % MgO) near the subaerial summit. They interpreted that these primitive magmas erupted on the flank, thereby avoiding the main magma chamber. The same may be true for the Kibblewhite Volcano. We discovered magnesian andesites on the NE–SW trending fissure ridge of the flank but low-Mg andesites, dacites, and rhyolites near the summit (Fig. 3). This suggests that the magnesian andesites erupted through the fissure, thereby avoiding the main magma chamber. Therefore, we believe that it may be possible to discover magnesian andesites by sampling the flanks of other frontal volcanoes in the Kermadec arc.

CONCLUSION

This study investigated the origin of magnesian andesites from the Kibblewhite Volcano in the Kermadec arc. The magnesian andesites are aphyric and olivine saturated, indicating that they were not produced by disequilibrium processes such as magma mixing, crystal accumulation, and crustal contamination. The estimated primary magma compositions of the magnesian andesites compare similarly to that of the HMAs observed in other subduction zones. Trace element and isotopic characteristics in the magnesian andesites are typical of volcanic rocks in the Kermadec arc, suggesting that the subduction of a young plate or melting of a pyroxenitic source is not necessary to produce magnesian andesites. Instead, we propose that the magnesian andesites were produced by the direct melting of the uppermost mantle of the Kermadec arc. These results support the hypothesis that primary andesitic magmas generate in a volcanic arc where the crust is thin. If primary andesitic magmas are usually generated in the Kermadec arc, scientists will be forced to reconsider the current understanding of magma genesis in the Kermadec arc, based on a basaltic source material. However, it is difficult to make generalizations based on this study alone; to corroborate the findings of this study, it is important to find HMAs at other volcanoes in the Kermadec arc. To discover new HMAs, we advise collecting samples around the flanks of volcanoes rather than collecting samples at their summits.

FUNDING

This work was supported by JSPS KAKENHI grant no. 19J10691 to Y.H. and no. JP21H01195 to Y.T. We thank the German Federal Ministry of Education and Research (BMBF) (grant no. 03G0255A) for funding the R/V SONNE SO255 cruise.

DATA AVAILABILITY

The data underlying this article are available in its online supplementary material.

CONFLICT OF INTEREST

There is no conflict of interest.

Supplementary Data

Supplementary data are available at *Journal of Petrology* online.

ACKNOWLEDGEMENTS

We would like to thank the captains and crew of the R/V SONNE for their successful sampling. Georg Zellmer and Carl Spandler

are greatly thanked for editorial handling. We thank the two anonymous reviewers for their constructive reviews. We also acknowledge constructive discussions with Susumu Umino, Tomoaki Morishita, and Osamu Ishizuka. We are grateful to Weihong Zhang, Hiroko Higuchi, and Mitsuko Kanazawa for their analytical assistance in the measurement of trace elements and isotopic compositions. We thank A. Tame for their analytical assistance in the EPMA measurements.

References

Baker, M. B., Grove, T. L. & Price, R. (1994). Primitive basalts and andesites from the Mt. Shasta region, N. California: products of varying melt fraction and water content. *Contributions to Mineralogy and Petrology* **118**, 111–129. https://doi.org/10.1007/BF01052863.

Baker, J., Peate, D., Waight, T. & Meyzen, C. (2004). Pb isotopic analysis of standards and samples using a ^{207}Pb–^{204}Pb double spike and thallium to correct for mass bias with a double-focusing MC-ICP-MS. *Chemical Geology* **211**, 275–303. https://doi.org/10.1016/j.chemgeo.2004.06.030.

Barker, S. J., Wilson, C. J. N., Baker, J. A., Millet, M.-A., Rotella, M. D., Wright, I. C. & Wysoczanski, R. J. (2013). Geochemistry and petrogenesis of silicic magmas in the intra-oceanic Kermadec arc. *Journal of Petrology* **54**, 351–391. https://doi.org/10.1093/petrology/egs071.

Barsdell, M. (1988). Petrology and petrogenesis of clinopyroxene-rich tholeiitic lavas, Merelava volcano, Vanuatu. *Journal of Petrology* **29**, 927–964. https://doi.org/10.1093/petrology/29.5.927.

Barsdell, M. & Berry, R. F. (1990). Origin and evolution of primitive island arc ankaramites from Western Epi, Vanuatu. *Journal of Petrology* **31**, 747–777. https://doi.org/10.1093/petrology/31.3.747.

Bassett, D., Kopp, H., Sutherland, R., Henrys, S., Watts, A. B., Timm, C., Scherwath, M., Grevemeyer, I. & de Ronde, C. E. J. (2016). Crustal structure of the Kermadec arc from MANGO seismic refraction profiles. *Journal of Geophysical Research - Solid Earth* **121**, 7514–7546. https://doi.org/10.1002/2016JB013194.

Birner, S. K., Warren, J. M., Cottrell, E., Davis, F. A., Kelley, K. A. & Falloon, T. J. (2017). Forearc peridotites from tonga record heterogeneous oxidation of the mantle following subduction initiation. *Journal of Petrology* **58**, 1755–1780. https://doi.org/10.1093/petrology/egx072.

Blatter, D. L. & Carmichael, I. S. E. (1998). Plagioclase-free andesites from Zitácuaro (Michoacán), Mexico: petrology and experimental constraints. *Contributions to Mineralogy and Petrology* **132**, 121–138. https://doi.org/10.1007/s004100050411.

Bowman, E. E. & Ducea, M. N. (2023). Pyroxenite melting at subduction zones. *Geology* **51**, 383–386. https://doi.org/10.1130/G50929.1.

Bryant, J. A., Yogodzinski, G. M. & Churikova, T. G. (2011). High-Mg# andesitic lavas of the Shisheisky Complex, Northern Kamchatka: implications for primitive calc-alkaline magmatism. *Contributions to Mineralogy and Petrology* **161**, 791–810. https://doi.org/10.1007/s00410-010-0565-4.

Calvert, A. J., Klemperer, S. L., Takahashi, N. & Kerr, B. C. (2008). Three-dimensional crustal structure of the Mariana island arc from seismic tomography. *Journal of Geophysical Research* **113**, 1–24. https://doi.org/10.1029/2007JB004939.

Chang, Q., Shibata, T., Shinotsuka, K., Yoshikawa, M. & Tatsumi, Y. (2003). Precise determination of trace elements in geological standard rocks using inductively coupled plasma mass spectrometry (ICP-MS). *Frontier Research on Earth Evolution* **1**, 357–362.

Cole, J. W., Thordarson, T. & Burt, R. M. (2000). Magma origin and evolution of White Island (Whakaari) volcano, Bay of Plenty, New Zealand. *Journal of Petrology* **41**, 867–895. https://doi.org/10.1093/petrology/41.6.867.

Contreras-Reyes, E., Grevemeyer, I., Watts, A. B., Flueh, E. R., Peirce, C., Moeller, S. & Papenberg, C. (2011). Deep seismic structure of the Tonga subduction zone: implications for mantle hydration, tectonic erosion, and arc magmatism. *Journal of Geophysical Research* **116**, 1–18. https://doi.org/10.1029/2011JB008434.

Crawford, A. J., Falloon, T. J. & Green, D. H. (1989). Classification, petrogenesis and tectonic setting of boninites. *Boninites and Related Rocks* , 2–49.

Defant, M. J. & Drummond, M. S. (1990). Derivation of some modern magmas through melting of young subducted lithosphere. *Nature* **347**, 662–665. https://doi.org/10.1038/347662a0.

Elliott, T. (2003). Tracers of the slab inside the subduction factory. *Geophysical Monograph Series* **128**, 23–45.

Ewart, A., Bryan, W. B., Chappell, B. W. & Rudnick, R. L. (1994). 24. Regional geochemistry of the Lau-Tonga arc and backarc systems. *Proceedings of the Ocean Drilling Program: Scientific Results* **135**, 385–425.

Ewart, A., Collerson, K. D., Regelous, M., Wendt, J. I. & Niu, Y. (1998). Geochemical evolution within the Tonga-Kermadec-Lau arc-back-arc systems: the role of varying mantle wedge composition in space and time. *Journal of Petrology* **39**, 331–368. https://doi.org/10.1093/petroj/39.3.331.

Gaetani, G. A. & Grove, T. L. (1998). The influence of water on melting of mantle peridotite. *Contributions to Mineralogy and Petrology* **131**, 323–346. https://doi.org/10.1007/s004100050396.

Gamble, J. A., Wright, I. C. & Baker, J. A. (1993). Seafloor geology and petrology in the oceanic to continental transition zone of the Kermadec-Havre-Taupo Volcanic Zone arc system, New Zealand. *New Zealand Journal of Geology and Geophysics* **36**, 417–435. https://doi.org/10.1080/00288306.1993.9514588.

Gamble, J., Woodhead, J. O. N., Wright, I. A. N. & Smith, I. A. N. (1996). Basalt and sediment geochemistry and magma petrogenesis in a transect from oceanic island arc to rifted continental margin arc: the Kermadec-Hikurangi margin, SW Pacific. *Journal of Petrology* **37**, 1523–1546. https://doi.org/10.1093/petrology/37.6.1523.

Gamble, J. A., Christie, R. H. K., Wright, I. C. & Wysoczanski, R. J. (1997). Primitive K-rich magmas from Clark Volcano, southern Kermadec Arc; a paradox in the K-depth relationship. *Canadian Mineralogist* **35**, 275–290.

Gill, J. B. (1981). Orogenic andesites and plate tectonics. *Minerals, Rocks and Mountains* . https://doi.org/10.1007/978-3-642-68012-0.

Gill, J., Hoernle, K., Todd, E., Hauff, F., Werner, R., Timm, C., Garbe-Schönberg, D. & Gutjahr, M. (2021). Basalt geochemistry and mantle flow during early Backarc Basin evolution: Havre trough and Kermadec arc, Southwest Pacific. *Geochemistry, Geophysics, Geosystems* **22**(GC009339), e2020. https://doi.org/10.1029/2020GC009339.

Grove, T. L. & Till, C. B. (2019). Rich mantle melting near the slab–wedge interface. *Contributions to Mineralogy and Petrology* **174**, 1–22. https://doi.org/10.1007/s00410-019-1615-1.

Grove, T., Parman, S., Bowring, S., Price, R. & Baker, M. (2002). The role of an H_2O-rich fluid component in the generation of primitive basaltic andesites and andesites from the Mt. Shasta region, N California. *Contributions to Mineralogy and Petrology* **142**, 375–396. https://doi.org/10.1007/s004100100299.

Grove, T. L., Elkins-Tanton, L. T., Parman, S. W., Chatterjee, N., Müntener, O. & Gaetani, G. A. (2003). Fractional crystallization and mantle-melting controls on calc-alkaline differentiation trends. *Contributions to Mineralogy and Petrology* **145**, 515–533. https://doi.org/10.1007/s00410-003-0448-z.

Haase, K. M., Worthington, T. J., Stoffers, P., Garbe-Schönberg, D. & Wright, I. (2002). Mantle dynamics, element recycling, and magma genesis beneath the Kermadec Arc-Havre Trough. *Geochemistry, Geophysics, Geosystems* **3**, 1–22. https://doi.org/10.1029/2002GC000335.

Haase, K. M., Krumm, S., Regelous, M., Joachimski, M. & Isl, R. (2011). Oxygen isotope evidence for the formation of silicic Kermadec island arc and Havre–Lau backarc magmas by fractional crystallisation. *Earth and Planetary Science Letters* **309**, 348–355. https://doi.org/10.1016/j.epsl.2011.07.014.

Hart, S. R., Gerlach, D. C. & White, W. M. (1986). A possible new Sr-Nd-Pb mantle array and consequences for mantle mixing. *Geochimica et Cosmochimica Acta* **50**, 1551–1557. https://doi.org/10.1016/0016-7037(86)90329-7.

Hauff, F., Hoernle, K., Gill, J., Werner, R., Timm, C., Garbe-Schönberg, D., Gutjahr, M. & Jung, S. (2021). R/V Sonne cruise SO255 "VITIAZ": an integrated major element, trace element and Sr-Nd-Pb-Hf isotope data set of volcanic rocks from the Colville and Kermadec ridges, the Quaternary Kermadec volcanic front and the Havre Trough backarc basin, version 1.0. *Interdisciplinary Earth Data Alliance (IEDA)* . https://doi.org/10.26022/IEDA/111723.

Heyworth, Z., Turner, S., Schaefer, B., Wood, B., George, R., Berlo, K., Cunningham, H., Price, R., Cook, C. & Gamble, J. (2007). ^{238}U-^{230}Th-^{226}Ra-^{210}Pb constraints on the genesis of high-Mg andesites at White Island, New Zealand. *Chemical Geology* **243**, 105–121. https://doi.org/10.1016/j.chemgeo.2007.05.012.

Hirai, Y., Yoshida, T., Okamura, S., Tamura, Y., Sakamoto, I. & Shinjo, R. (2018). Breakdown of residual zircon in the Izu arc subducting slab during backarc rifting. *Geology* **46**, 371–374. https://doi.org/10.1130/G39856.1.

Hirose, K. & Kushiro, I. (1993). Partial melting of dry peridotites at high pressures: determination of compositions of melts segregated from peridotite using aggregates of diamond. *Earth and Planetary Science Letters* **114**, 477–489. https://doi.org/10.1016/0012-821X(93)90077-M.

Hirschmann, M. M., Baker, M. B. & Stolper, E. M. (1998). The effect of alkalis on the silica content of mantle-derived melts. *Geochimica et Cosmochimica Acta* **62**, 883–902. https://doi.org/10.1016/S0016-7037(98)00028-3.

Hoernle, K., Hauff, F., van den Bogaard, P., Werner, R., Mortimer, N., Geldmacher, J., Garbe-Schönberg, D. & Davy, B. (2010). Age and geochemistry of volcanic rocks from the Hikurangi and Manihiki oceanic plateaus. *Geochimica et Cosmochimica Acta* **74**, 7196–7219. https://doi.org/10.1016/j.gca.2010.09.030.

Hoernle, K., Hauff, F. & Werner, R. (2017). RV SONNE Fahrtbericht: cruise report So255: VITIAZ—The life cycle of the Vitiaz-Kermadec arc/backarc system: from arc initiation to splitting and backarc basin formation. GEOMAR Report N. Ser. 03. 386.

Hoernle, K., Gill, J., Timm, C., Hauff, F., Werner, R., Garbe-Schönberg, D. & Gutjahr, M. (2021). Hikurangi Plateau subduction a trigger for Vitiaz arc splitting and Havre Trough opening (southwestern Pacific). *Geology* **49**, 536–540. https://doi.org/10.1130/G48436.1.

Kanayama, K., Umino, S. & Ishizuka, O. (2012). Eocene volcanism during the incipient stage of Izu-Ogasawara Arc: geology and petrology of the Mukojima Island Group, the Ogasawara Islands. *Island Arc* **21**, 288–316. https://doi.org/10.1111/iar.12000.

Kelemen, P. B. (1995). Genesis of high Mg# andesites and the continental crust. *Contributions to Mineralogy and Petrology* **120**, 1–19. https://doi.org/10.1007/BF00311004.

Kelemen, P. B., Hanghøj, K. & Greene, A. R. (2003a). One view of the geochemistry of subduction-related magmatic arcs, with an emphasis on primitive andesite and lower crust. *Treatise on Geochemistry* , 2–70.

Kelemen, P. B., Yogodzinski, G. M. & Scholl, D. W. (2003b). Along-strike variation in the Aleutian island arc: genesis of high Mg # andesite. *Inside the subduction factory*. *Geophysical Monograph Series* **138**, 223–276. https://doi.org/10.1029/138GM11.

Kimura, J. I., Sisson, T. W., Nakano, N., Coombs, M. L. & Lipman, P. W. (2006). Isotope geochemistry of early Kilauea magmas from the submarine Hilina bench: the nature of the Hilina mantle component. *Journal of Volcanology and Geothermal Research* **151**, 51–72. https://doi.org/10.1016/j.jvolgeores.2005.07.024.

Kodaira, S., Sato, T., Takahashi, N., Miura, S., Tamura, Y., Tatsumi, Y. & Kaneda, Y. (2007). New seismological constraints on growth of continental crust in the Izu-Bonin intra-oceanic arc. *Geology* **35**, 1031–1034. https://doi.org/10.1130/G23901A.1.

Kuno, H. (1968). Origin of andesite and its bearing on the island arc structure. *Bulletin Volcanologique* **32**, 141–176. https://doi.org/10.1007/BF02596589.

Kushiro, I. (1969). The system forsterite-diopside-silica with and without water at high-pressures. *American Journal of Science* **267A**, 269–294.

Kushiro, I. (1972). Determination of liquidus relations in synthetic silicate systems with electron probe analysis: the system forsterite-diopside-silica at 1 atmosphere. *American Mineralogist* .

Kushiro, I. (1996). Partial melting of a fertile mantle peridotite at high pressures: an experimental study using aggregates of diamond. *Geophysical Monograph Series* **95**, 109–122. https://doi.org/10.1029/GM095p0109.

Larter, R. D., Vanneste, L. E., Morris, P. & Smythe, D. K. (2003). Structure and tectonic evolution of the South Sandwich arc. *Geological Society, London, Special Publications* **219**, 255–284. https://doi.org/10.1144/GSL.SP.2003.219.01.13.

Leake, B. E. *et al.* (1997). Nomenclature of amphiboles: report of the subcommittee on amphiboles of the international mineralogical association, commission on new minerals and mineral names. *American Mineralogist* **82**, 1019–1037.

le Maitre, R. W. (2002) *Igneous Rocks: A Classification and Glossary of Terms: Recommendations of the International Union of Geological Sciences, Subcommission on the Systematics of Igneous Rocks*. Cambridge: Cambridge University Press.

Sun, S.-S. & McDonough, W. F. (1989). Chemical and isotopic systematics of oceanic basalts: implications for mantle composition and processes. *Geological Society, London, Special Publications* **42**, 313–345. https://doi.org/10.1144/GSL.SP.1989.042.01.19.

McDonough, W. F. & Sun, S. S. (1995). The composition of the Earth. *Chemical Geology* **120**, 223–253. https://doi.org/10.1016/0009-2541(94)00140-4.

Mitchell, A. L. & Grove, T. L. (2015). Melting the hydrous, subarc mantle: the origin of primitive andesites. *Contributions to Mineralogy and Petrology* **170**, 1–23. https://doi.org/10.1007/s00410-015-1161-4.

Miyashiro, A. (1974). Volcanic rock series in island arcs and active continental margins. *American Journal of Science* **274**, 321–355. https://doi.org/10.2475/ajs.274.4.321.

Miyazaki, T., Vaglarov, B. S., Takei, M., Suzuki, M., Suzuki, H., Ohsawa, K., Chang, Q., Takahashi, T., Hirahara, Y., Hanyu, T., Kimura, J., Tatsumi, Y., Miyazaki, T., Stefanov Vaglarov, B., Takei, M., Suzuki, M., Suzuki, H., Ohsawa, K., Chang, Q. & Tatsumi, Y. (2012). Development of a fully automated open-column chemical-separation system-COLUMNSPIDER-and its application to Sr-Nd-Pb isotope analyses of igneous rock samples. *Journal of Mineralogical and Petrological Sciences* **107**, 74–86. https://doi.org/10.2465/jmps.110520.

Miyazaki, T., Hanyu, T., Kimura, J., Senda, R., Vaglarov, B. S., Chang, Q., Hirahara, Y., Takahashi, T., Kawabata, H. & Sato, T. (2018). Clinopyroxene and bulk rock Sr–Nd–Hf–Pb isotope compositions

of Raivavae Ocean island basalts: does clinopyroxene record early stage magma chamber processes? *Chemical Geology* **482**, 18–31. https://doi.org/10.1016/j.chemgeo.2017.12.015.

Morgan, G. B. & London, D. (1996). Optimizing the electron microprobe analysis of hydrous alkali aluminosilicate glasses. *American Mineralogist* **81**, 1176–1185. https://doi.org/10.2138/am-1996-9-1016.

Mortimer, N. & Parkinson, D. (1996). Hikurangi Plateau: a cretaceous large igneous province in the Southwest Pacific Ocean. *Journal of Geophysical Research: Solid Earth* **101**, 687–696. https://doi.org/10.1029/95JB03037.

Nishizawa, T., Nakamura, H., Churikova, T., Gordeychik, B., Ishizuka, O., Haraguchi, S., Miyazaki, T., Vaglarov, B. S., Chang, Q., Hamada, M., Kimura, J. I., Ueki, K., Toyama, C., Nakao, A. & Iwamori, H. (2017). Genesis of ultra-high-Ni olivine in high-Mg andesite lava triggered by seamount subduction. *Scientific Reports* **7**, 11515. https://doi.org/10.1038/s41598-017-10276-3.

Ohba, T., Kimura, Y. & Fujimaki, H. (2007). High-magnesian andesite produced by two-stage magma mixing: a case study from Hachimantai, Northern Honshu, Japan. *Journal of Petrology* **48**, 627–645. https://doi.org/10.1093/petrology/egl075.

Patchett, P. J. & Tatsumoto, M. (1981). Lu/hf in chondrites and definition of a chondritic hafnium growth curve. *Lunar and Planetary Science* ***XII*** , 822–824.

Pearce, J. A., Kempton, P. D. & Gill, J. B. (2007). Hf-Nd evidence for the origin and distribution of mantle domains in the SW Pacific. *Earth and Planetary Science Letters* **260**, 98–114. https://doi.org/10.1016/j.epsl.2007.05.023.

Rapp, R. P., Shimizu, N., Norman, M. D. & Applegate, G. S. (1999). Reaction between slab-derived melts and peridotite in the mantle wedge: experimental constraints at 3.8 GPa. *Chemical Geology* **160**, 335–356. https://doi.org/10.1016/S0009-2541(99)00106-0.

Rapp, R. P., Norman, M. D., Laporte, D., Yaxley, G. M., Martin, H. & Foley, S. F. (2010). Continent formation in the archean and chemical evolution of the cratonic lithosphere: melt-rock reaction experiments at 3–4 GPa and petrogenesis of Archean Mg-diorites (Sanukitoids). *Journal of Petrology* **51**, 1237–1266. https://doi.org/10.1093/petrology/egq017.

de Ronde, C. E. J., Baker, E. T., Massoth, G. J., Lupton, J. E., Wright, I. C., Sparks, R. J., Bannister, S. C., Reyners, M. E., Walker, S. L., Greene, R. R., Ishibashi, J., Faure, K., Resing, J. A. & Lebon, G. T. (2007). Submarine hydrothermal activity along the mid-Kermadec Arc, New Zealand: large-scale effects on venting. *Geochemistry, Geophysics, Geosystems* **8**. https://doi.org/10.1029/2006GC001495.

Rudnick, R. L. & Gao, S. (2003). Composition of the continental crust. *Treatise on Geochemistry* , 1–64. https://doi.org/10.1016/B0-08-043751-6/03016-4.

Ruscitto, D. M., Wallace, P. J. & Kent, A. J. R. (2011). Revisiting the compositions and volatile contents of olivine-hosted melt inclusions from the Mount Shasta region: implications for the formation of high-Mg andesites. *Contributions to Mineralogy and Petrology* **162**, 109–132. https://doi.org/10.1007/s00410-010-0587-y.

Shukuno, H., Tamura, Y., Tani, K., Chang, Q., Suzuki, T. & Fiske, R. S. (2006). Origin of silicic magmas and the compositional gap at Sumisu submarine caldera, Izu-Bonin arc, Japan. *Journal of Volcanology and Geothermal Research* **156**, 187–216. https://doi.org/10.1016/j.jvolgeores.2006.03.018.

Smith, I. E. M., Stewart, R. B. & Price, R. C. (2003a). The petrology of a large intra-oceanic silicic eruption: the Sandy Bay Tephra, Kermadec Arc, Southwest Pacific. *Journal of Volcanology and Geothermal Research* **124**, 173–194. https://doi.org/10.1016/S0377-0273(03)00040-4.

Smith, I. E. M., Worthington, T. J., Stewart, R. B., Price, R. C. & Gamble, J. A. (2003b). Felsic volcanism in the Kermadec arc, SW Pacific: crustal recycling in an oceanic setting. *Geological Society, London, Special Publications* **219**, 99–118. https://doi.org/10.1144/GSL.SP.2003.219.01.05.

Smith, I. E. M., Worthington, T. J., Price, R. C., Stewart, R. B. & Maas, R. (2006). Petrogenesis of dacite in an oceanic subduction environment: Raoul Island, Kermadec arc. *Journal of Volcanology and Geothermal Research* **156**, 252–265. https://doi.org/10.1016/j.jvolgeores.2006.03.003.

Smith, I. E. M., Stewart, R. B., Price, R. C. & Worthington, T. J. (2010). Are arc-type rocks the products of magma crystallisation? Observations from a simple oceanic arc volcano: Raoul Island, Kermadec Arc, SW Pacific. *Journal of Volcanology and Geothermal Research* **190**, 219–234. https://doi.org/10.1016/j.jvolgeores.2009.05.006.

Sobolev, A. V., Hofmann, A. W., Sobolev, S. V. & Nikogosian, I. K. (2005). An olivine-free mantle source of Hawaiian shield basalts. *Nature* **434**, 590–597. https://doi.org/10.1038/nature03411.

Straub, S. M., LaGatta, A. B., Martin-Del Pozzo, A. L. & Langmuir, C. H. (2008). Evidence from high-Ni olivines for a hybridized peridotite/pyroxenite source for orogenic andesites from the central Mexican Volcanic Belt. *Geochemistry, Geophysics, Geosystems* **9**. https://doi.org/10.1029/2007GC001583.

Straub, S. M., Gomez-Tuena, A., Stuart, F. M., Zellmer, G. F., Espinasa-Perena, R., Cai, Y. & Iizuka, Y. (2011). Formation of hybrid arc andesites beneath thick continental crust. *Earth and Planetary Science Letters* **303**, 337–347. https://doi.org/10.1016/j.epsl.2011.01.013.

Straub, S. M., Zellmer, G. F., Gómez-Tuena, A., Espinasa-Pereñ, A. R., Martin-Del Pozzo, A. L., Stuart, F. M. & Langmuir, C. H. (2014). A genetic link between silicic slab components and calc-alkaline arc volcanism in Central Mexico. *Geological Society Special Publication* **385**, 31–64. https://doi.org/10.1144/SP385.14.

Streck, M. J. & Leeman, W. P. (2018). Petrology of "Mt. Shasta" high-magnesian andesite (HMA): a product of multi-stage crustal assembly. *American Mineralogist* **103**, 216–240. https://doi.org/10.2138/am-2018-6151.

Streck, M. J., Leeman, W. P. & Chesley, J. (2007). High-magnesian andesite from Mount Shasta: a product of magma mixing and contamination, not a primitive mantle melt. *Geology* **35**, 351–354. https://doi.org/10.1130/G23286A.1.

Syracuse, E. M., van Keken, P. E., Abers, G. A., Suetsugu, D., Bina, C., Inoue, T., Wiens, D. & Jellinek, M. (2010). The global range of subduction zone thermal models. *Physics of the Earth and Planetary Interiors* **183**, 73–90. https://doi.org/10.1016/j.pepi.2010.02.004.

Takahashi, N., Kodaira, S., Klemperer, S. L., Tatsumi, Y., Kaneda, Y. & Suyehiro, K. (2007). Crustal structure and evolution of the Mariana intra-oceanic island arc. *Geology* **35**, 203–206. https://doi.org/10.1130/G23212A.1.

Tamura, Y. & Tatsumi, Y. (2002). Remelting of an andesitic crust as a possible origin for rhyolitic magma in oceanic arcs: an example from the Izu–Bonin arc. *Journal of Petrology* **43**, 1029–1047. https://doi.org/10.1093/petrology/43.6.1029.

Tamura, Y., Ishizuka, O., Stern, R., Nichols, A. R. L., Kawabata, H., Hirahara, Y., Chang, Q., Miyazaki, T., Kimura, J. I., Embley, R. W. & Tatsumi, Y. (2014). Mission immiscible: distinct subduction components generate two primary magmas at Pagan Volcano, Mariana Arc. *Journal of Petrology* **55**, 63–101. https://doi.org/10.1093/petrology/egt061.

Tamura, Y., Sato, T., Fujiwara, T., Kodaira, S. & Nichols, A. (2016). Advent of continents: a new hypothesis. *Scientific Reports* **6**, 33517. https://doi.org/10.1038/srep33517.

Tamura, Y., Ishizuka, O., Sato, T. & Nichols, A. R. L. (2019). Nishinoshima volcano in the Ogasawara Arc: New continent from the ocean? *Island Arc* **28**, e12285. https://doi.org/10.1111/iar.12285.

Tani, K., Kawabata, H., Chang, Q., Sato, K. & Tatsumi, Y. (2005). Quantitative analyses of silicate rock major and trace elements by X-ray fluorescence spectrometer: evaluation of analytical precision and sample preparation. *Frontier Research on Earth Evolution* **2**, 1–8.

Tatsumi, Y. (1982). Origin of high-magnesian andesites in the Setouchi volcanic belt, Southwest Japan, II. Melting phase relations at high pressures. *Earth and Planetary Science Letters* **60**, 305–317. https://doi.org/10.1016/0012-821X(82)90009-7.

Tatsumi, Y. & Hanyu, T. (2003). Geochemical modeling of dehydration and partial melting of subducting lithosphere: toward a comprehensive understanding of high-Mg andesite formation in the Setouchi volcanic belt, SW Japan. *Geochemistry, Geophysics, Geosystems* **4**, 1–19. https://doi.org/10.1029/2003GC000530.

Tatsumi, Y. & Ishizaka, K. (1982). Origin of high-magnesian andesites in the Setouchi volcanic belt, Southwest Japan, I. Petrographical and chemical characteristics. *Earth and Planetary Science Letters* **60**, 293–304. https://doi.org/10.1016/0012-821X(82)90008-5.

Taylor, S. R. (1967). The origin and growth of continents. *Tectonophysics* **4**, 17–34. https://doi.org/10.1016/0040-1951(67)90056-X.

Taylor, S. R. & McLennan, S. M. (1995). The geochemical evolution of the continental crust. *Reviews of Geophysics* **33**, 241. https://doi.org/10.1029/95RG00262.

Taylor, R. N., Nesbitt, R. W., Vidal, P., Harmon, R. S., Auvray, B. & Croudace, I. W. (1994). Mineralogy, chemistry, and genesis of the boninite series volcanics, Chichijima, Bonin Islands, Japan. *Journal of Petrology* **35**, 577–617. https://doi.org/10.1093/petrology/35.3.577.

Timm, C., Davy, B., Haase, K., Hoernle, K. A., Graham, I. J., de Ronde, C. E. J., Woodhead, J., Bassett, D., Hauff, F., Mortimer, N., Seebeck, H. C., Wysoczanski, R. J., Caratori-Tontini, F. & Gamble, J. A. (2014). Subduction of the oceanic Hikurangi Plateau and its impact on the Kermadec arc. *Nature Communications* **5**, 4923. https://doi.org/10.1038/ncomms5923.

Timm, C., Leybourne, M. I., Hoernle, K., Wysoczanski, R. J., Hauff, F., Handler, M., Caratori Tontini, F. C. & de Ronde, C. E. J. (2016). Trench-perpendicular geochemical variation between two adjacent Kermadec arc volcanoes Rumble II East and West: the role of the subducted Hikurangi Plateau in element recycling in arc magmas. *Journal of Petrology* **57**, 1335–1360. https://doi.org/10.1093/petrology/egw042.

Timm, C., de Ronde, C. E. J., Hoernle, K., Cousens, B., Wartho, J.-A., Tontini, F. C., Wysoczanski, R., Hauff, F. & Handler, M. (2019). New age and geochemical data from the southern Colville and Kermadec Ridges, SW Pacific: insights into the recent geological history and petrogenesis of the Proto-Kermadec (Vitiaz) Arc. *Gondwana Research* **72**, 169–193. https://doi.org/10.1016/j.gr.2019.02.008.

Todd, E., Gill, J. B., Wysoczanski, R. J., Handler, M. R., Wright, I. C. & Gamble, J. A. (2010). Sources of constructional cross-chain volcanism in the southern Havre trough: new insights from HFSE and REE concentration and isotope systematics. *Geochemistry, Geophysics, Geosystems* **11**. https://doi.org/10.1029/2009GC002888.

Todd, E., Gill, J. B., Wysoczanski, R. J., Hergt, J., Wright, I. C., Leybourne, M. I. & Mortimer, N. (2011). Hf isotopic evidence for small-scale heterogeneity in the mode of mantle wedge enrichment: southern Havre Trough and South Fiji Basin back arcs. *Geochemistry, Geophysics, Geosystems* **12**. https://doi.org/10.1029/2011GC003683.

Tollstrup, D. L. & Gill, J. B. (2005). Hafnium systematics of the Mariana arc: evidence for sediment melt and residual phases. *Geology* **33**, 737–740. https://doi.org/10.1130/G21639.1.

Turner, S., Hawkesworth, C., Rogers, N., Bartlett, J., Worthington, T., Hergt, J., Pearce, J. & Smith, I. (1997). ^{238}U-^{230}Th disequilibria, magma petrogenesis, and flux rates beneath the depleted Tonga-Kermadec island arc. *Geochimica et Cosmochimica Acta* **61**, 4855–4884. https://doi.org/10.1016/S0016-7037(97)00281-0.

Umino, S. (1986). Magma mixing in boninite sequence of Chichijima, Bonin Islands. *Journal of Volcanology and Geothermal Research* **29**, 125–157. https://doi.org/10.1016/0377-0273(86)90042-9.

Vervoort, J. D. & Blichert-Toft, J. (1999). Evolution of the depleted mantle: Hf isotope evidence from juvenile rocks through time. *Geochimica et Cosmochimica Acta* **63**, 533–556. https://doi.org/10.1016/S0016-7037(98)00274-9.

Walter, M. J. & Presnall, D. C. (1994). Melting behavior of simplified lherzolite in the system CaO-MgO-Al_2O_3-SiO_2-Na_2O from 7 to 35 kbar. *Journal of Petrology* **35**, 329–359. https://doi.org/10.1093/petrology/35.2.329.

Warren, J. M. (2016). Global variations in abyssal peridotite compositions. *Lithos* **248-251**, 193–219. https://doi.org/10.1016/j.lithos.2015.12.023.

Wood, B. J. (2004). Melting of fertile peridotite with variable amounts of H_2O. *Geophysical Monograph Series* **150**, 69–80. https://doi.org/10.1029/150GM07.

Wood, B. J. & Turner, S. P. (2009). Origin of primitive high-Mg andesite: constraints from natural examples and experiments. *Earth and Planetary Science Letters* **283**, 59–66. https://doi.org/10.1016/j.epsl.2009.03.032.

Wright, I. C., Worthington, T. J. & Gamble, J. A. (2006). New multibeam mapping and geochemistry of the 30°–35° S sector, and overview, of southern Kermadec arc volcanism. *Journal of Volcanology and Geothermal Research* **149**, 263–296. https://doi.org/10.1016/j.jvolgeores.2005.03.021.

Yogodzinski, G. M., Volynets, O. N., Koloskov, A. V., Seliverstov, N. I. & Matvenkov, V. V. (1994). Magnesian andesites and the subduction component in a strongly calc-alkaline series at Piip volcano, far western Aleutians. *Journal of Petrology* **35**, 163–204. https://doi.org/10.1093/petrology/35.1.163.

Yogodzinski, G. M., Kay, R. W., Volynets, O. N. V., Koloskov, A. V. & Kay, S. M. (1995). Magnesian andesite in the western Aleutian Komandorsky region: implications for slab melting and processes in the mantle wedge. *Geological Society of America Bulletin* **107**, 505–519. https://doi.org/10.1130/0016-7606(1995)107<0505:MAITWA>2.3.CO;2.

Yogodzinski, G. M., Brown, S. T., Kelemen, P. B., Vervoort, J. D., Portnyagin, M., Sims, K. W. W., Hoernle, K., Jicha, B. R. & Werner, R. (2015). The role of subducted basalt in the source of Island Arc magmas: evidence from seafloor lavas of the Western Aleutians. *Journal of Petrology* **56**, 441–492. https://doi.org/10.1093/petrology/egv006.